# Measurement of Proton and Nitrogen Polarization in Ammonia and a Test of Equal Spin Temperature

*The Spin Muon Collaboration*

## Abstract

The 1996 data taking of the SMC experiment used polarized protons to measure the spin dependent structure function $g_1$ of the proton. Three liters of solid granular ammonia were irradiated at the Bonn electron linac in order to create the paramagnetic radicals which are needed for polarizing the protons. Proton polarizations of $\pm(90 \pm 2.5)\,\%$ were routinely reached. An analysis based on a theoretical line-shape for spin-1 systems with large quadrupolar broadening was developed which allowed the nitrogen polarization in the ammonia to be determined with a $10\,\%$ relative error. The measured quadrupolar coupling constant of $^{14}$N agrees well with earlier extrapolated values. The polarization of the nitrogen nuclei was measured as a function of the proton polarization in order to provide a test of the equal spin temperature (EST) hypothesis. It was found to be closely valid under the dynamic nuclear polarization conditions with which the protons are polarized. Large deviations from EST could be induced by cross relaxing the proton and nitrogen spin systems at low fields. Nitrogen polarizations up to 40% were reached by these means.

B. Adeva[18], E. Arik[2], A. Arvidson[21], B. Badelek[21,23], G. Baum[1], P. Berglund[8], L. Betev[13], N. de Botton[17], F. Bradamante[20], C. Bradtke[3], A. Bravar[11], S. Bültmann[22], D. Crabb[22], J. Cranshaw[20], T. Çuhadar[2], S. Dalla Torre[20], R. van Dantzig[15], B. Derro[4], A. Deshpande[24], S. Dhawan[24], C. Dulya[15,p], H. Dutz[3,f], S. Eichblatt[n], D. Fasching[16,m], F. Feinstein[17], C. Fernandez[18,9], S. Forthmann[7], B. Frois[17], A. Gallas[18], J. A. Garzon[18,9], R. Gehring[3], H. Gilly[6], M. Giorgi[20], S. Goertz[3], G. Gracia[18], N. de Groot[15,l], M. Grosse Perdekamp[24], K. Haft[13], J. Harmsen[3], D. von Harrach[11], T. Hasegawa[14,b], P. Hautle[5,a], N. Hayashi[14,c], C. A. Heusch[5,e], N. Horikawa[14], V. W. Hughes[24], G. Igo[4], S. Ishimoto[14,d], T. Iwata[14], E. M. Kabuß[11], T. Kageya[14], A. Karev[10], T. J. Ketel[15], J. Kiryluk[23], Yu. Kisselev[10], E. Kok[15], D. Krämer[1], W. Kröger[5,e], K. Kurek[23], J. Kyynäräinen[1,8], M. Lamanna[20], U. Landgraf[6], J. M. Le Goff[17], F. Lehar[17], A. de Lesquen[17], J. Lichtenstadt[19], M. Litmaath[15,i], A. Magnon[17], G. K. Mallot[11], A. Martin[20], T. Matsuda[14,b], B. Mayes[9], J. S. McCarthy[22], K. Medved[10], W. Meyer[3], G. van Middelkoop[15], D. Miller[16], Y. Miyachi[14], K. Mori[14], J. Nassalski[23], T. O. Niinikoski[5], J. E. J. Oberski[15], A. Ogawa[14], D. P. Parks[9], H. Pereira da Costa[17], F. Perrot-Kunne[17], D. Peshekhonov[10], L. Pinsky[9], S. Platchkov[17], M. Plo[18], M. Plückthun[3], J. Polec[23], D. Pose[10], H. Postma[15], J. Pretz[11], R. Puntaferro[20], G. Rädel[5], G. Reicherz[3], A. Rijllart[5], M. Rodriguez[21], E. Rondio[23,5], A. Sandacz[23], I. Savin[10], P. Schiavon[20], A. Schiller[7,o], E. P. Sichtermann[15], F. Simeoni[20], G. I. Smirnov[10], A. Staude[13], A. Steinmetz[11], U. Stiegler[5], H. Stuhrmann[7], F. Tessarotto[20], W. Tlaczala[23,k], A. Tripet[1], G. Unel[2], M. Velasco[16,i], J. Vogt[13], R. Voss[5], C. Whitten[4], R. Windmolders[12], W. Wislicki[23], A. Witzmann[6], J. Ylöstalo[8], A. M. Zanetti[20], K. Zaremba[23,j]

[1] University of Bielefeld, Physics Department, 33501 Bielefeld, Germany[aa]
[2] Bogaziçi University and Istanbul Technical University, Istanbul University, Istanbul, Turkey[bb]
[3] University of Bochum, Physics Department, 44780 Bochum, Germany[aa]
[4] University of California, Department of Physics, Los Angeles, 90024 CA[cc]
[5] CERN, 1211 Geneva 23, Switzerland
[6] University of Freiburg, Physics Department, 79104 Freiburg, Germany[aa]
[7] GKSS, 21494 Geesthacht, Germany[aa]
[8] Helsinki University of Technology, Low Temperature Laboratory and Institute of Particle Physics Technology, 02150 Espoo, Finland
[9] University of Houston, Physics Department, Houston, 77204-5504 TX[cc]
[10] JINR, Laboratory of Particle Physics, Dubna, Russia
[11] University of Mainz, Institute for Nuclear Physics, 55099 Mainz, Germany[aa]
[12] University of Mons, Faculty of Science, 7000 Mons, Belgium
[13] University of Munich, Physics Department, 80799 Munich, Germany[aa]
[14] Nagoya University, CIRSE and Department of Physics, Furo-Cho, Chikusa-Ku, 464 Nagoya, Japan[ee]
[15] NIKHEF, Delft University of Technology, FOM and Free University, 1009 AJ Amsterdam, The Netherlands[ff]
[16] Northwestern University, Department of Physics, Evanston, 60208 IL[cc,dd]
[17] C.E.A. Saclay, DAPNIA, 91191 Gif-sur-Yvette, France[gg]
[18] University of Santiago, Department of Particle Physics, 15706 Santiago de Compostela, Spain[hh]
[19] Tel Aviv University, School of Physics, 69978 Tel Aviv, Israel[ii]
[20] INFN Trieste and University of Trieste, Department of Physics, 34127 Trieste, Italy
[21] Uppsala University, Department of Radiation Sciences, 75121 Uppsala, Sweden
[22] University of Virginia, Department of Physics, Charlottesville, 22901 VA[cc]
[23] Soltan Institute for Nuclear Studies and Warsaw University, 00681 Warsaw, Poland[jj]
[24] Yale University, Department of Physics, New Haven, 06511 CT[cc]
[a] Permanent address: Paul Scherrer Institut, 5232 Villigen, Switzerland
[b] Permanent address: Miyazaki University, Faculty of Engineering, 889-21 Miyazaki-Shi, Japan
[c] Permanent address: The Institute of Physical and Chemical Research (RIKEN), wako 351-01, Japan
[d] Permanent address: KEK, Tsukuba-Shi, 305 Ibaraki-Ken, Japan
[e] Permanent address: University of California, Institute of Particle Physics, Santa Cruz, 95064 CA
[f] Permanent address: University of Bonn, Physics Institute, 53115 Bonn, Germany
[n] Permanent address: Fermi National Accelerator Laboratory, Batavia, 60510 IL
[k] Permanent address: Institute of Physics, Warsaw University of Technology.
[j] Permanent address: Institute of Radioelectronics, Warsaw University of Technology.
[i] Now at CERN, 1211 Geneva 23, Switzerland
[l] Now at SLAC, Stanford, 94309 CA
[p] Now at Asosiación EUROTOM/CIEMAT para fusión, Avda Complutense 22, 28040, Madrid, Spain
[m] Now at Physics Department, University of Wisconsin, Madison, WI
[o] Now at University of Oslo, Physics Department, N-0316 Oslo 3, Norway

# 1    Introduction

The measurement of spin dependent structure functions requires that both the target and the beam be polarized. At CERN, the Spin Muon Collaboration (SMC) used a beam of muons polarized to about 80 % and targets of polarized protons and deuterons with polarizations of about 90 % and 50 %, respectively [1, 2, 3, 4, 5]. Before 1996, SMC used normal or fully deuterated butanol as target material. Butanol is a clean material to use in polarized targets in the sense that the background carbon and oxygen nuclei are spinless. However, the dilution factor, which is the relative amount of polarizable nucleons in the material, is rather small for butanol. In 1996, we used an ammonia target in order to further investigate the spin structure of the proton. Ammonia has a much larger dilution factor than butanol, but it has the drawback that its nitrogen nuclei have spin-1 and introduce a polarized background. Thus, the polarization of the nitrogen nuclei must be known before the spin structure functions can be extracted from the data. The Equal Spin Temperature (EST) hypothesis allows the nitrogen polarization to be written as a function of the proton polarization. Were it valid, the nitrogen polarization could be calculated from the measured proton polarization and the lengthy process of measuring nitrogen polarization during the limited beam time of SMC would not be necessary.

There have been other investigations of the EST hypothesis in ammonia. It was concluded [7] that EST seems to hold well in $^{14}NH_3$ up to $\pm 80\%$ proton polarizations. In $^{14}ND_3$ an EST between the nitrogen nuclei and the deuterons was found, but for the residual protons a strong disagreement was observed [8]. In $^{15}NH_3$ and in $^{15}ND_3$ there are conflicting results, even when exactly same material was used [7, 8, 9, 10]. Because of these disagreements and because higher polarizations than $\pm 80\%$ were expected, we decided to measure the nitrogen polarization as carefully as possible.

This paper is organized as follows: §2 describes the preparation of the ammonia material for use as a polarized target, and §3 discusses the technique of polarization measurement. §4 covers the results of the proton polarization measurement and error analysis. §5 develops a nitrogen line-shape, discusses the method of measuring the nitrogen NMR signals, and presents the results of the nitrogen polarization measurement. §6 concerns the relationship between the proton and nitrogen polarizations in ammonia and the effect of the polarized nitrogen nuclei on the measurement of the proton spin structure functions.

## 1.1    General Target Description

The target [6] consisted of two volumes, each a 65 cm long cylinder with a diameter of 5 cm, which are referred to as the "upstream" and "downstream" target cells. The ammonia material was in the form of small granules which were cooled with a dilution refrigerator. The protons of the ammonia in the two target cells were dynamically polarized [11] in opposite ways, either parallel or antiparallel to the beam momentum direction. The beam was polarized antiparallel to its momentum. Thus, both beam-target polarization configurations were available simultaneously. To further aid in reducing acceptance effects of the spectrometer to the two target cells, the spin directions of the protons in the target halves were reversed five times per day by "rotating" the magnetic field in an automated procedure. The solenoid field was lowered from 2.5 T and raised again with the opposite polarity while a transverse field of 0.5 T was applied when the solenoid field decreased below 0.5 T. This procedure only required that the the muon beam be turned off for 10 minutes. In addition to the field rotations, the polarizations

of the cells were reversed by dynamic nuclear polarization (DNP) at three week intervals.

The proton polarization was measured using NMR at four sampling points in each target cell. Before and after the data run of SMC, the nitrogen polarization was measured as a function of proton polarization using one NMR coil.

## 1.2 The Choice of Ammonia as the Target Material

The statistical error on the measurement of the proton spin dependent structure function for a given amount of beam time shows the following dependencies on material properties

$$\sigma \propto \frac{1}{\sqrt{x \rho \kappa} P} \tag{1}$$

where $P$ is the average nucleon polarization, $\rho$ is the density, $x$ is the packing fraction, and $\kappa$ is the dilution factor of the material. In the first approximation, the dilution factor is just the fraction of polarizable nucleons and thus yields $\kappa_{amm} = 3/17$ and $\kappa_{but} = 10/74$. The average polarization obtained by SMC in the 1993 data taking was $P_{but} = \pm 86\%$ whereas the average polarization reached in 1996 was $P_{amm} = \pm 89\%$. The solid densities of the two materials at 77 K are $\rho_{amm} = 0.853$ g/cm$^3$ [12] and $\rho_{but} = 0.985$ g/cm$^3$ [13]. The effective density $x\rho$ was also smaller for ammonia than butanol because the ammonia granules had irregular shapes, and, in addition, are only slightly denser than liquid nitrogen. This presents handling difficulties since the target cells are submersed in a liquid nitrogen bath during packing. The ammonia packing fraction was measured to be only 0.58 whereas it was 0.63 in the butanol target [13]. Using these values, the ratio of statistical errors of the measurements on ammonia compared to those on butanol is

$$\frac{\sigma_{amm}}{\sigma_{but}} \approx 0.82 \sqrt{\frac{x_{but}}{x_{amm}}} \frac{P_{but}}{P_{amm}} \approx 0.83 \ .$$

To reach the same statistical accuracy with a butanol target, about 45% more beam time would have been needed.

## 2 Material Preparation

This section explains the preparation of the liquid ammonia for use as a polarized proton target. About 2 kg of ammonia with a purity of 99.98% and the natural isotope content was used as the raw material. It was delivered as liquid with a vapor pressure of 8.6 bar at a temperature of 293 K. At 1 bar, the boiling point of ammonia is 240 K and its melting point is 195 K. Its gaseous state density is 0.719 g/cm$^3$ at 288 K and its liquid state density is 0.682 g/cm$^3$ at 240 K.

## 2.1 Solidification and Granulation

The liquefied gas can be solidified either in a fast or in a slow process which have both been shown to provide highly polarizable material. In the fast solidification, liquid ammonia is dropped into liquid nitrogen which leads to spherical frozen beads. With this procedure a large amount of solid material can be produced in a reasonable time. However, due to the fast solidification the beads are brittle and their density is ill-defined because of the inclusion of bubbles. Both disadvantages are serious because the ammonia beads tend to disintegrate during the subsequent irradiation and, therefore, there is a considerable uncertainty in the determination of the target density. This fast freezing procedure was chosen for the target material of the EMC experiment [14]. In the slow process, the gaseous ammonia is liquefied and thereafter slowly frozen in the same glass tube. Using this method, a solid block of frozen ammonia is obtained which has only a few crystal domains. Then, this block is crushed and sieved to obtain chips of the desired size (2-3 mm). Granules made in this way are more stable and uniform.
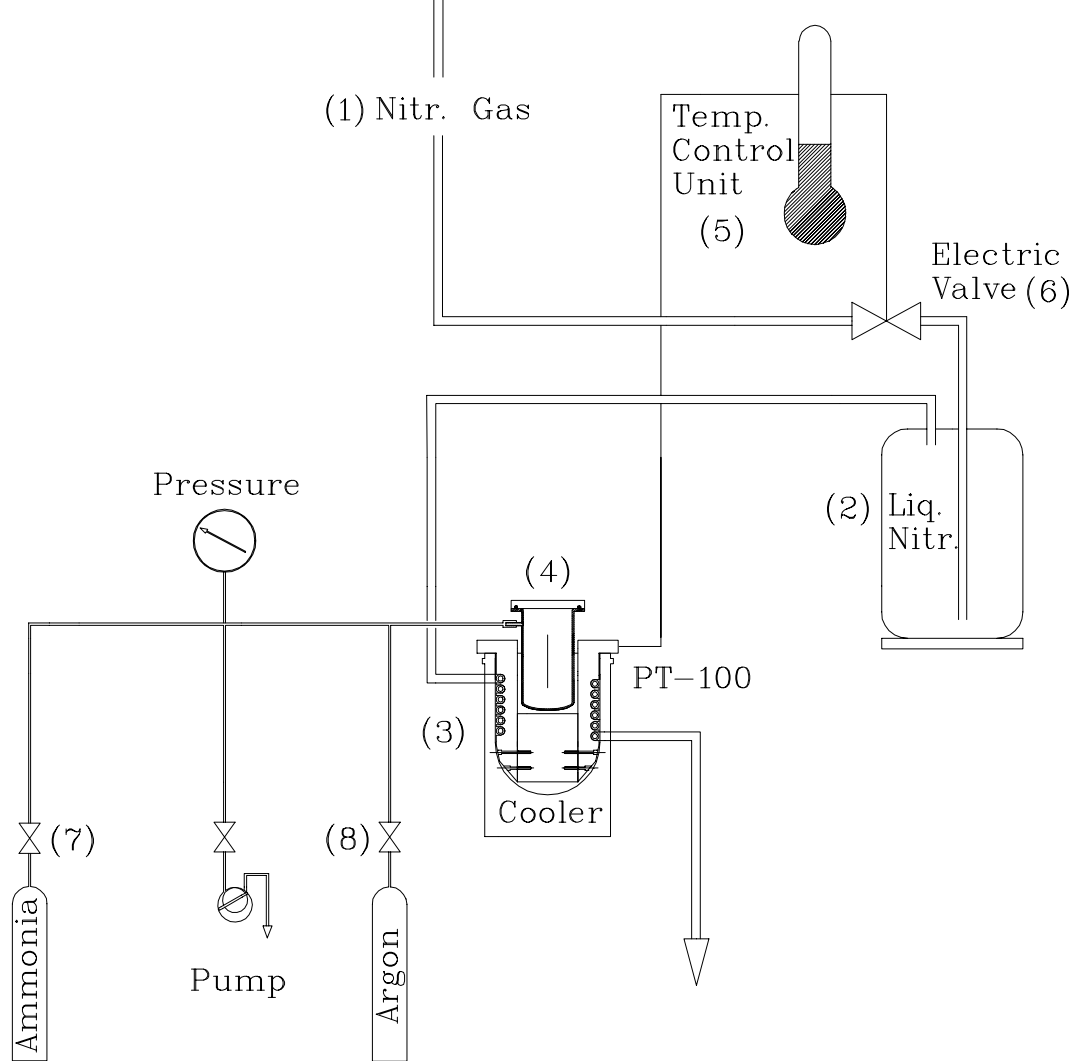
Figure 1: The solidification apparatus for the ammonia material. Its operation is described in the text.

A new high-capacity solidification apparatus with a continuous cooling system was constructed. As shown in Fig. 1, nitrogen gas (1) was cooled by guiding it through a liquid nitrogen vessel (2). The gas passed through a heat exchanger which was immersed in an ethanol bath (3) surrounding a glass tube (4). The temperature of the bath, monitored by a Pt100 resistor and regulated (5) to within $\pm 1^\circ$ C, controlled the nitrogen flow rate (6). Ammonia gas was condensed in the glass tube as soon as the temperature of the cooling bath decreased below 240 K. The condensing pressure was stabilized at 500 mbar. The desired bath temperature of about 190 K was typically reached within 1 hour. The ammonia gas inlet (7) was closed after about 150 cm$^3$ of ammonia was liquefied. The material immediately started to freeze from the outer regions towards the center. At the same time, the vapor pressure was decreasing towards the triple point of about 60 mbar. In this stage the glass cylinder was filled with 500 mbar of argon (8). This allowed the liquid to freeze homogeneously and the final product was a clear and transparent block of solid ammonia. After removing the lid, the cylinder was filled with liquid nitrogen which caused the material to crack. Finally, it was crushed into pieces and sifted to the desired chip size at 77 K. Each solidification process took 6 hours and resulted in 125 cm$^3$ of 2-3 mm size ammonia chips which were stored in liquid nitrogen until the irradiation.

## 2.2 Production of the Paramagnetic Centers

For the DNP process to operate efficiently, a paramagnetic center density on the order of $10^{19}\,e^-/\mathrm{cm}^3$ is needed. In the case of irradiated ammonia, these centers are $\dot{\mathrm{N}}\mathrm{H}_2$ radicals, which were identified via electron paramagnetic resonance studies [15]. The radicals were created by irradiating the solid ammonia chips in the 20 MeV electron beam at the Bonn linac. The average beam current was 30 $\mu$A. The irradiation was carried out in several batches of 100 cm$^3$ each. During the irradiation, a special cryostat kept the sample in a liquid argon bath at 87 K. The details of an earlier version of this cryostat are described in Ref. [14]. In order to achieve similar conditions for all batches, some parts of the cryostat were improved. The most significant concern was ensuring that in each batch an equal amount of homogeneously distributed paramagnetic centers were created. Thus, the geometry of the sample container and the conditions and control of the material exposure to the electron beam were optimized.

Fig. 2 shows a schematic diagram of the apparatus with a detailed view of the sample container. The cryostat consisted of a thermally isolated inner part (1) containing the argon, which was liquefied by a liquid nitrogen heat exchanger (2). The argon level (3) is indicated by the shaded area. Since at 1 bar, the boiling and freezing points (87.3 K, 83.8 K) of argon are close, the temperature of the argon coolant in the sample container (4) was kept constant by controlling the liquid nitrogen level in the heat exchanger with the argon vapor pressure. From energy loss estimations of the electron beam, the expected heating power was several hundred watts, which agreed well with a calculation based on the liquid nitrogen consumption of the heat exchanger.

The sample container was a frame of two concentric cylinders made of aluminum and covered with thin titanium foils (6). It was fixed to a rotating aluminum shaft (7). A current integrator (8) which measured the flow of electrons emitted by the material and captured by the container walls was connected by a rotating feed-through (5) to the sample container. The integrated current was used as a relative measure for the density of the paramagnetic centers. The geometry of the container, in combination with the vertically spread beam spot (9) and the 1 rps rotation speed of the sample, produced a sufficiently homogeneous irradiation of the material. A maximum of 150 cm$^3$ of material could be irradiated uniformly in a single run. The homogeneity was determined from the uniform violet color of the granules produced by the irradiation as well as from the similar polarization behavior of different small samples which were tested at Bonn. The accurate bombarding current could not be measured due to the unknown amount of secondary electron emission. Thus, the amount of integrated current ($10^{17}e^-/\mathrm{cm}^2$) that the batches were requested to receive was inferred from the polarization behavior of several test batches which received different amounts of irradiation. The final density of the paramagnetic centers was estimated to be $6\times10^{19}$ cm$^{-3}$ from previous measurements [15].

## 3 Measurement of Polarization

The measurement of polarization was based on integrating the absorptive part of the RF susceptibility $\chi''$, which can be related to the polarization by [17]

$$P \equiv \frac{\langle I_z \rangle}{I} = \frac{2\hbar I}{g^2 \mu_N^2 N \pi} \int_0^\infty \chi''(\omega)\,\mathrm{d}\omega \tag{2}$$

where $\mu_N$ is the nuclear magneton, $I$ and $g$ are the spin and $g$-factor of the species, and $N$ is the number of spins in the sample. This equation is not generally valid when quadrupolar interactions are present. The effect for nitrogen is discussed in §5.6 and corrections are estimated.

Using Eq. (2) to determine the $^{14}$N polarization involves two important practical difficulties as well. The NMR signal is too broad to be covered with a single frequency sweep and it is too small for a direct calibration. The first problem was solved by measuring two small pieces
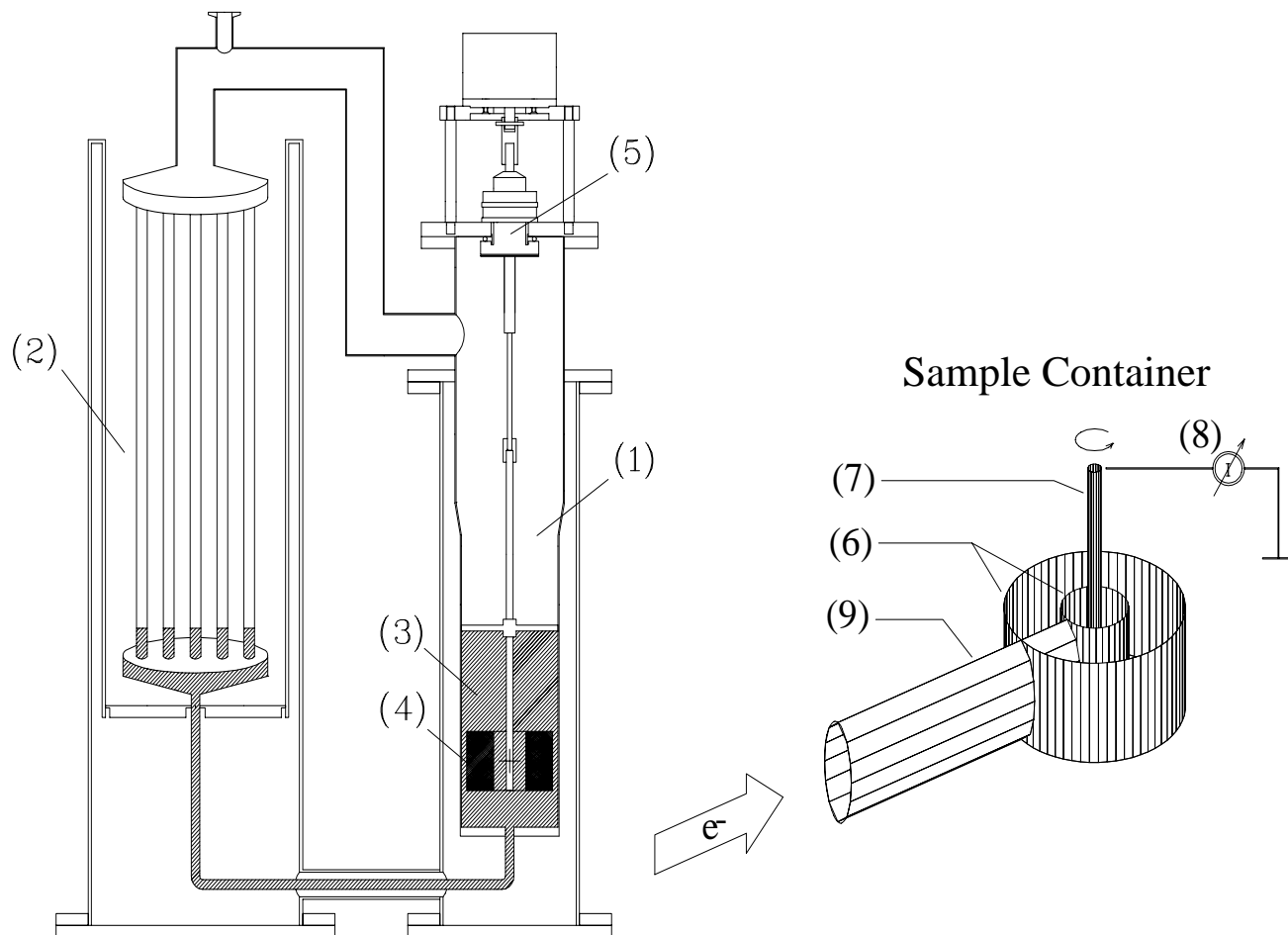
Figure 2: Schematics of the irradiation cryostat on the left and the sample container detail on the right.

of the nitrogen signal and reconstructing the whole signal by fitting a theoretical line-shape to the data. From this signal, the unnormalized area could be calculated. The calibration of the NMR system was done using proton signals taken at the nitrogen Larmor frequency.

The quadrupolar splitting of the nitrogen NMR line provides a second method to determine the polarization, which could be used as a verification of the results. The shape of the resonance line depends on polarization in a way which will be described in §5.1.

## 3.1  Equal Spin Temperature

The DNP process in ammonia, with a high density of paramagnetic centers and the EPR line width larger than the nuclear Larmor frequency, is believed [7, 15] to proceed mainly via cooling of the electron spin-spin interaction reservoir which, in turn, is in strong thermal contact with the nuclear spins. This leads to an equal spin temperature ($T_s$) among all the polarizable spin species, assuming the spin-lattice relaxation and polarization time constants are equal for all nuclei. This is the EST hypothesis and it may be a plausible assumption in ammonia.

Ammonia contains both hydrogen and nitrogen nuclei which have spin-$\frac{1}{2}$ and spin-1, respectively. Let us show how their polarizations are linked if the two species have a common
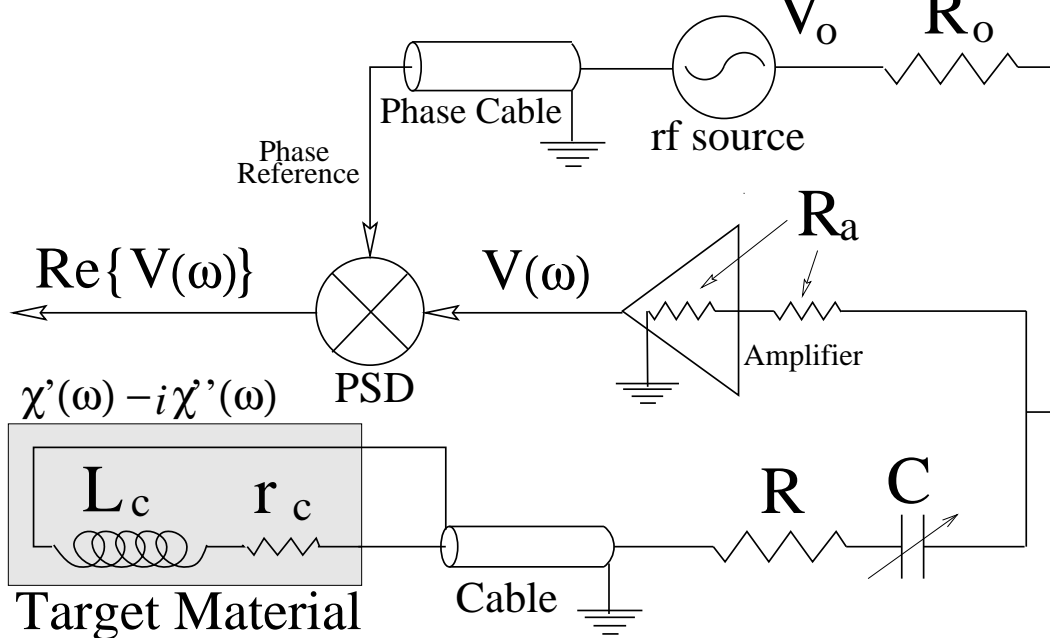
Figure 3: A block diagram of the NMR circuit. The rms excitation level $V_0$ was 100 mV.

spin temperature. The polarization of the proton system is written

$$P_{\mathrm{p}} = \tanh\left(\frac{\hbar\omega_{\mathrm{p}}}{2kT_{\mathrm{s}}}\right) \ . \tag{3}$$

where $\omega_{\mathrm{p}}$ is the Larmor angular frequency of protons. In the absence of quadrupolar interactions, the polarization of a spin-1 nitrogen system is

$$P_{\mathrm{N}} = \frac{4\tanh\left(\frac{\hbar\omega_{\mathrm{N}}}{2kT_{\mathrm{s}}}\right)}{3 + \tanh^2\left(\frac{\hbar\omega_{\mathrm{N}}}{2kT_{\mathrm{s}}}\right)} = \frac{r^2 - 1}{r^2 + r + 1} \tag{4}$$

where $r = e^{\hbar\omega_{\mathrm{N}}/kT_{\mathrm{s}}}$ and $\omega_{\mathrm{N}}$ is the nitrogen Larmor angular frequency. Assuming EST is valid, the polarizations of the two systems are related by

$$P_{\mathrm{N}} = \frac{4\tanh\left(\frac{\omega_{\mathrm{N}}}{\omega_{\mathrm{p}}}\mathrm{arctanh}(P_{\mathrm{p}})\right)}{3 + \tanh^2\left(\frac{\omega_{\mathrm{N}}}{\omega_{\mathrm{p}}}\mathrm{arctanh}(P_{\mathrm{p}})\right)} \ . \tag{5}$$

Due to the quadrupolar splitting, Eq. (4) is not exact. The corrections involved in the estimation of the polarization including the quadrupolar broadening as a perturbation are, however, small for the nitrogen system being considered here. The calculations are made in §5.6.

## 3.2  The NMR Instrumentation

Measuring the polarization by NMR was done using commercially available Q-meters [24], each connected to an NMR coil via a coaxial cable, a capacitor, and a damping resistor forming a series LRC circuit. The circuit, shown in Fig. 3, is driven by a digitally controlled frequency synthesizer. As the frequency is swept through the Larmor resonance, the material absorbs or emits energy causing a change in the inductance of the coil. The inductance change, in turn, causes an impedance change in the circuit, of which the complex output voltage, $V(\omega, \chi)$, is a function as long as the feed current is kept constant. At the last stage, a phase sensitive detector (PSD) allows the selection of the real part of the output with respect to a reference fed in from the synthesizer.

The procedure for measuring a signal follows. First, the magnetic field is set such that
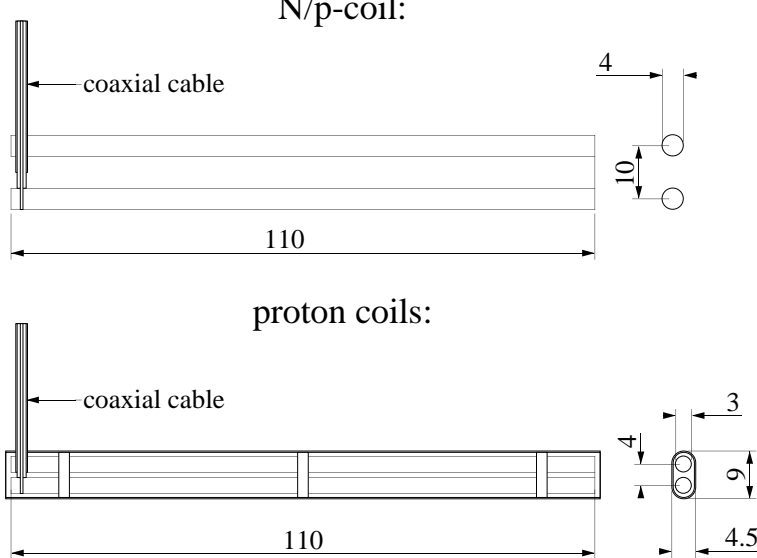
7

## N/p-coil:



## proton coils:



Figure 4: The NMR coils as used in the SMC 1996 data taking. The N/p-coil was used to measure both proton and nitrogen polarization, and the other coils were used for protons only. The coils were made of CuNi tube with a wall thickness of about 0.1 mm. The proton coils were enclosed in an FEP/PTFE sheat.

the Larmor frequency of the spin species is not within the sweep range of the synthesizer. This measures the frequency dependence of the output voltage to the NMR electronics, which is denoted by $\mathrm{Re}\{V_o(\omega)\}$, and is called the Q-curve. Next, the field is set to the resonance value and the output voltage is measured again, which is denoted by $\mathrm{Re}\{V(\omega)\}$. Then, the Q-curve is subtracted from it and the result is called a subtracted signal. The absorption function of the material is proportional to the subtracted signal,

$$\chi''(\omega) \propto \mathrm{Re}\{V(\omega)\} - \mathrm{Re}\{V_o(\omega)\} \equiv S(\omega),$$

and, therefore, the polarization is proportional to the integral of that signal,

$$P \propto \int_{\Delta\omega} S(\omega)\mathrm{d}\omega,$$

where $\Delta\omega$ is the frequency range over which the signal is measured. The small residual Q-curve, owing to circuit drift between the two measurements, is taken care of by fitting a polynomial to the signal wings, and by subtracting it. The absolute calibration of the system is done by comparing the signal area to a known polarization value when the material is at thermal equilibrium (TE) at about 1 K temperature.

During the "field rotation" procedure, the proton Larmor frequency is also swept over a broad range. When the polarization is negative, during field ramping it is possible to induce superradiance [25] which destroys, or even reverses, the polarization locally around the NMR coil, due to the circuit self-resonances. To overcome this effect, small-inductance coils were used to avoid those circuit resonances which lie at proton Larmor frequencies swept through during the rotation procedure.

The coils intended for measuring only proton polarization were entirely enclosed in an FEP/PTFE sheat to reduce the filling factor, and thereby, the sensitivity of the coils. This was done in order to help prevent superradiance and, more importantly, to linearize the Q-meter response while measuring proton signals (see §4.2).

The design of the NMR coils is shown in Fig. 4 and the parameters of the NMR system are listed in Table 1. Because the coils could not be changed after loading of the target material and

| Parameter | Symbol | proton coils | N/p-coil Protons | N/p-coil Nitrogen |
|---|---|---|---|---|
| Larmor frequency (at 2.5 T) (MHz) | $\nu_\circ$ | 106.5 | 106.5 | 7.7 |
| Frequency sweep width (kHz) | $\Delta\nu$ | 600 | 600 | $2 \times 200$ or 300 |
| Feed resistance ($\Omega$) | $R_\circ$ | 900 | 1430 | 900 |
| Damping resistance ($\Omega$) | $R$ | 16 | 43 | 10 |
| Amplifier input impedance ($\Omega$) | $R_a$ | $50 + 70$ | $50+50$ | $50 + 60$ |
| Coil RF resistance (at $\nu_\circ$) ($\Omega$) | $r_c$ | 0.5 | 0.4 | 0.1 |
| Coil inductance (nH) | $L_c$ | 66 | 95 | 95 |
| Tuning capacitance (pF) | $C$ | 27 | 19 | 400 |
| Cable length in $\lambda/2$ (m) | $n$ ($\ell$) | 5 (5.0) | 5 (5.0) | 0.36 (5.0) |
| Cable Q-factor | $Q$ | 70 | 70 | 100 |
| Coil filling factor | $\eta$ | 0.14 | 0.29 | 0.29 |

Table 1: Typical circuit parameters for the proton and the nitrogen NMR system. The filling factor has been calculated assuming a homogeneous packing fraction of the material to be 0.6.

since both positive and negative polarizations were used simultaneously, we could not design the coils for optimal nitrogen signal detection. Otherwise, with the high-inductance coils necessary, superradiance and nonlinearity would have seriously handicapped the field rotation procedure and the polarization measurement. Thus, we modified only one coil so that it could be used (not optimized) for measuring both nitrogen and proton signals. This coil, labeled "N/p-coil", had a slightly higher inductance, and did not have a coating so that its sensitivity would be higher. The dual purpose coil was connected to different Q-meters with different cables depending on whether proton or nitrogen signals were being measured.

A novel technique was employed in the NMR system for measuring the nitrogen signals. Instead of a tuned $\lambda/2$ cable, a short ($\ell = 5\,\mathrm{m}$) untuned coaxial cable was used to connect the coil to the Q-meter. In this way the Q-curve becomes flatter and the effect of circuit drifts is diminished, including thermal drifts in the cable itself. The requirement is that the cable length should not be too close to the impedance pole that occurs at $\lambda/4 = 6.9\,\mathrm{m}$. All of the cables consisted of three sections, a 0.050" copper cable (Coaxitube DA50050) inside the mixing chamber, an 0.085" copper-clad stainless steel cable (Coaxitube JN50085) in the target holder and a 0.141" copper cable outside the cryostat.

## 4    Proton Polarization

In this section, we present the results of the proton polarization measurement. A simple model of the proton NMR line-shape in ammonia is developed so that corrections for the non-linearity of the Q-meters could be made. Then, the complete error analysis which considers both TE and enhanced polarization signals is presented. The polarization characteristics of the ammonia material are demonstrated at the end.

### 4.1    Proton NMR Signal

Typical proton NMR signals for positive and negative polarizations are shown in Fig. 5 for low and high, positive and negative polarizations. The line-shape at low polarizations is symmetric but it becomes strongly asymmetric at the highest polarizations, and the peak shifts in different directions depending on the polarization sign.

The broadening of the line due to the inhomogeneity of the external field, which is on the order of $\Delta B/B = 3 \cdot 10^{-5}$, is small. The irregular shape of the granules gives rise to additional broadening due to the demagnetization field. This can be a larger effect than that due to the

field inhomogeneity, but it also leads to a symmetric broadening, as does the dipolar interaction in the crystalline lattice. Proton-nitrogen and nitrogen-nitrogen interactions are much weaker owing the small magnetic moment of the nitrogen. It was verified that the line-shapes were the same for two proton signals of $P_p = 90\,\%$ where the nitrogen polarizations were $P_N = 15\,\%$ and $P_N = 40\,\%$ (see §6.2).
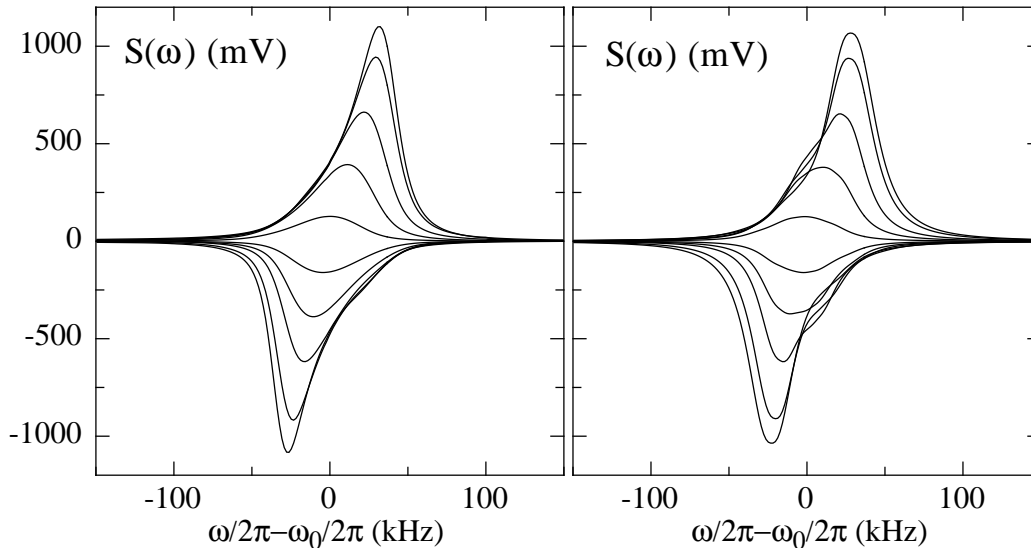


Figure 5: Proton NMR line-shapes. *Left*: Experimental proton line-shape for approximately $\pm 20$, $\pm 40$, $\pm 60$, $\pm 80$, and $\pm 90\%$ polarization. *Right*: The proton model line-shape for the same polarization values.

The line-shape due to dipolar interactions for a triangular configuration of nuclei has been calculated in Ref. [27]. The Zeeman levels with a $z$-component of total angular momentum $j = \pm\frac{1}{2}$ are threefoldly split while the level $j = \pm\frac{3}{2}$ are shifted. The resulting NMR line has contributions from 9 transitions between these sublevels whose energies depend on the relative orientation of the molecule with respect to the external field. Their calculation was unfortunately made only at zero polarization and is rather complicated.

Indirect spin-spin interactions can give rise to asymmetric line-shapes as well. They originate either from the distortion of the electron shell [16] or from exchange coupling of the s–state valence electrons [26]. In the ammonia molecule, the hydrogen atoms have covalent bonds with the nitrogen atom but not with each other. Therefore, the possible exchange interaction has to be mediated by the nitrogen.

Our goal was to develop a simple line-shape model in order to use it to study the properties of Q-meter circuit. It was based on the Hamiltonian for the indirect coupling between spins $\vec{I}_1$ and $\vec{I}_2$ which is of the form $\vec{I}_1 \cdot \vec{I}_2$. When applied to the triangular configuration of the protons it leads to two extra lines located symmetrically on each side of the Zeeman line. Only dipolar broadening due to next-nearest neighbors was included since indirect couplings are of much shorter range. Therefore, the full line was composed of three Gaussians. These three lines correspond to the $\mathcal{I}_+ (j = -\frac{3}{2} \rightarrow -\frac{1}{2})$, $\mathcal{I}_o (j = -\frac{1}{2} \rightarrow \frac{1}{2})$, and the $\mathcal{I}_- (j = \frac{1}{2} \rightarrow \frac{3}{2})$ transitions, where $j$ is the $z$-component of the total spin of the three protons.

The relative intensities can be easily calculated if we assume that the probability of individual spins having $I_z = \frac{1}{2}$ or $I_z = -\frac{1}{2}$ does not depend on the spin-spin interactions. This

10

| Error Source | $|\delta P/P|$ (%) | |
|---|---|---|
| | N/p-coil | proton coils |
| Temperature | 0.3 | 0.3 |
| Circuit Drift | 1.5 | 1.3 |
| Proton Background | 0.1 | 0.8 |
| Field Polarity | 0.1 | 0.1 |
| Relaxation | 0.3 | 0.3 |
| Total | 1.6 | 1.6 |

Table 2: TE calibration errors.

yields for the relative populations of the $j$ states

$$n_j = \left(\frac{13}{4} - j^2\right)\left(\frac{1+P}{2}\right)^{2j}\left(\frac{1-P}{2}\right)^{3(3-j)}$$

where $P$ is the polarization. The transition intensities, which are calculated from $\mathcal{I}_{j_1 \to j_2} \propto \frac{dn_{j_1}}{dt} = n_{j_2}W_{j_2 \to j_1} - n_{j_1}W_{j_1 \to j_2}$, where $W$ is the combinational transition probability, become

$$\mathcal{I}_+ = \left(\frac{1+P}{2}\right)^2, \ \mathcal{I}_- = \left(\frac{1-P}{2}\right)^2,$$

$$\mathcal{I}_o = 2\left(\frac{1+P}{2}\right)\left(\frac{1-P}{2}\right).$$

The right–hand plot in Fig. 5 shows examples of proton lines calculated using this model for several values of polarization. This model reproduces the basic features of the proton line-shape in ammonia, but does not fit well to the data. However, used with a splitting of $\Delta\nu = 25\,\text{kHz}$ between the three resonance lines, it was good enough to analyze the nonlinearity of the NMR circuit response.

## 4.2   Determination of Proton Polarization

The calibration of the NMR system was carried out at 1 K with the dilution refrigerator filled with superfluid $^4$He to ensure uniform temperature throughout the target volume. This was essential because the temperature during the calibration was measured once per signal only at one end of the 150 cm long target holder, by means of a $^3$He vapor pressure manometer.

The TE signal areas were extracted by first shifting the field by $\pm 1.5\%$ to record three Q-curves and then measuring three resonance signals at the nominal field. Each signal/Q-curve was averaged over 2000 double frequency sweeps over the 600 kHz range, which took four minutes. The proton relaxation time was measured to be about 20 minutes at 1 K and 2.5 T. Therefore, while the signals were being taken, the TE polarization was still relaxing from its shifted value towards its nominal value. However, since the Q-curves and signals were recorded with field shifts symmetrically around the nominal field, the error due to the relaxation canceled out.

In proton NMR the abundance of free protons in many construction materials introduces a polarized background signal which has to be subtracted from the TE signal. In our case the target holder was constructed of various plastic materials, most notably of Kevlar which can absorb up to 4.5% of water. The background signal was measured before loading the ammonia and remeasured after unloading it. The background contributed about 7% of the TE signal area and was the same both before and after the run. This background and the circuit drift which caused uncertainty in area determination of the signal were the largest error sources in the calibration (see Table 2).

Quite different error sources had to be considered while dealing with the NMR signals of the dynamically polarized material. The response of the Q-meter becomes nonlinear at high

| Error Source | $\lvert\delta P/P\rvert$ (%) | |
| --- | --- | --- |
| | N/p-coil | proton coils |
| Nonlinearity | 2.2 | 0.2 |
| Off-Centering | 0.1 | 0.1 |
| Field Polarity | 0.1 | 0.3 |
| Circuit Drift | 0.2 | 0.2 |
| Cross-Talk | 0.2 | 0.2 |
| Saturation | 1.1 | 0.5 |
| *Total* | 2.5 | 0.8 |

Table 3: Enhanced signal errors.

signal levels. The measured line-shape and area depend on the sign of polarization in a way that positive polarizations are underestimated and negative polarizations are overestimated.

In our case, the nonlinearity was large only in the N/p-coil which was designed to have higher sensitivity for measuring the nitrogen signals. We have corrected for it by following the guidelines of Ref. [19]. The first step was to find the effective circuit parameters which correspond to the simplified circuit model shown in Fig. 3. This was done by fitting the simulated Q-meter response function derived from the circuit diagram (8 parameters) to the measured Q-curves. The next step was to simulate the NMR signal which, in the case of ammonia, is more complex than for materials having a symmetrical line-shape. We used the model described here in §4.1 and calibrated the signal amplitude by using TE signals for which the nonlinearity was negligible. The separation of the sublines and their broadening were deduced by fitting the simulated lines to real signals from the proton coils for which the nonlinearity was small. As the final step, the signal area using the simulated response of the Q-meter was compared to real data. It was found that for coil 2 the correction to be made was up to 8% while for the other coils it remained below 2% with a relative uncertainty of 20%.

Another small correction was made for the shift of NMR line due to the internal field. The response of the Q-meter is frequency dependent and enhances signals which are shifted towards higher frequencies. The correction was about 0.5% at the highest polarizations.

In addition, there were several small error sources. Some dependency of the TE and enhanced signal areas on the solenoid field direction was observed but the origin of this effect remained unknown. There was RF cross-talk between the target cells which was measured by polarizing only one cell and observing the NMR signals in the other. A depolarization effect by the RF field (NMR saturation) was found and was twice as large for the uncoated N/p-coil as for the others. Therefore, the polarization was measured only at 10 minute intervals and long periods without DNP were avoided.

The impact of the uncertainty due to the corrections, together with other error sources, is listed in Table 3. The total uncertainty becomes thus $\lvert\delta P/P\rvert = 3.0\%$ for the N/p-coil and 2.1% for the others.

For a scattering experiment it is important that the polarization be averaged in the same way as the muon beam samples the material. The muon beam averaged the polarization uniformly longitudinally and had a Gaussian intensity profile with a 12 mm effective radius, which is the radius at which the number of DIS events originating from inside and outside were equal. By using several NMR coils placed throughout the target cells, we were able to average the polarization longitudinally and verify that there were no large variations of polarization. The NMR coils (except the N/p-coil) were placed at the effective radius of the beam so that a linear radial gradient in the polarization could not cause a bias.

To estimate the uncertainty of the average polarization it was necessary to calculate the

12

volume sampled by each coil. The sampling is weighed by the square of the transverse RF field amplitude and thus drops rapidly with distance from the coil wire. The volume giving rise to 95% of the total NMR signal was calculated to be $75\,cm^3$ for the N/p-coil and $55\,cm^3$ for the others. Assuming random sampling of the polarization, the $1\sigma$ confidence limits became $|\delta P/P| = 2.2\%$ for the upstream target cell and 0.9% for the downstream one. The difference is due to one inoperative coil in the upstream cell and due to the more even polarization distribution in the downstream cell. The overall uncertainty of the proton polarization measurement, averaged over the target cells, became $|\delta P/P|=2.7\%$.
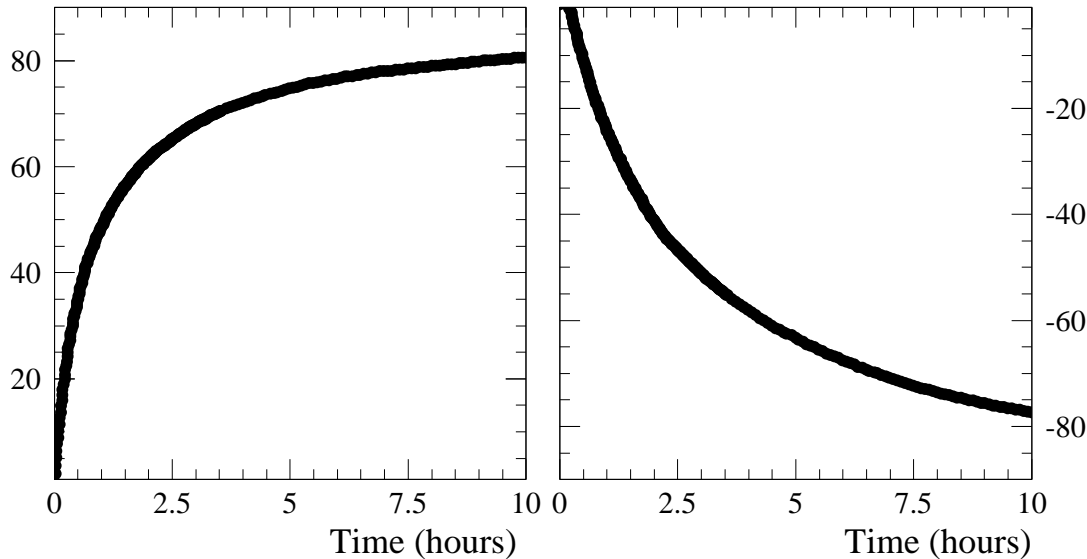


Figure 6: Simultaneous build-up curves for the two target cells. *Left*: Positive polarization in percent. *Right*: Negative polarization in percent.

## 4.3  Proton Polarization Characteristics

The material in the downstream target was prepared about half a year earlier than the material in the upstream and was stored for three months in liquid nitrogen and three months in liquid helium. There was a visible discoloration of the older material but its polarizability was the same as that of the newer ammonia.

The optimum microwave frequencies for polarizing positively and negatively were found to be 69.970 GHz and 70.350 GHz, respectively. In contrast to butanol, frequency modulation of the microwaves [30] led to only a small improvement of the dynamic polarization. The total increase owing to frequency modulation with an amplitude of 20 MHz and frequency of 1 kHz was estimated to be about 2% absolute.

About ±80 % polarization was obtained within 10 hours after starting DNP and maximum polarizations of ±90 % were reached. The maximum negative polarization was slightly higher than the positive polarization, but the difference was less than 2%. Fig. 6 shows the polarization rise in the upstream and the downstream half of the polarized target as a function of time for the first 10 hours of DNP. During the SMC data taking, the average polarization was ±89% which was very close to the maximum.

The spin-lattice relaxation times were longer in ammonia than in butanol, probably due to the lower density of paramagnetic centers. At 2.5 T and about 50 mK no thermal relaxation could be observed in 12 hours. At 0.5 T, which was the minimum field during the field rotations, the relaxation time was about 500 hours. This assured negligible losses during the field rotations. Interestingly, the decay time in zero field was about 1 hour at 70 mK. In addition, unless the

polarities of the solenoid magnet's correction coils were reversed during the field ramp to make the field inhomogeneous, strong superradiance effects were seen. A change of polarization from -89% to +28% was seen for some NMR coils.

## 5    Nitrogen Polarization

In this section, we present the results of the nitrogen polarization measurements. First, a theoretical line-shape is developed which can be fit to the two pieces of the NMR signals. From this, the nitrogen polarization can be determined from both the shape and integral of the signals. In addition, the line-shape allows a prediction of the dependence of the ratio of the nitrogen signal peak heights on polarization. The theoretical ratio is compared to values estimated from the raw signal data.

### 5.1    The Nitrogen Resonance Signal

The energy states of a spin-1 system held in a magnetic field, including interaction of the electric quadrupole moment and electric field gradients existing at the site of the nucleus, is, to first order in perturbation theory, [20]

$$E_m = -\hbar\omega_{\mathrm{N}}m - \hbar\omega_{\mathrm{q}}[3\cos^2(\theta) - 1](3m^2 - 2) \tag{6}$$

where $m = -1, 0, 1$ is the magnetic quantum number and $\omega_{\mathrm{q}} \equiv e^2 Qq/(8\hbar)$ is a measure of the quadrupole coupling strength. Here $Q$ and $eq$ are the quadrupole moment and the electric field gradient, respectively [21]. The sign of the quadrupole term has been chosen to have $\omega_{\mathrm{q}} > 0$ for ^{14}N in ammonia [23]. Axial symmetry of the field gradient about an axis which makes an angle $\theta$ with respect to the static field was assumed [22]. There are two lines in this system which have energies $\hbar\omega_+ = E_o - E_1$ and $\hbar\omega_- = E_{-1} - E_o$ and intensities $I_{\pm}$ which are proportional to the net number of spins available to make the transitions. For a given resonance frequency, the two lines correspond to the two angles

$$\cos(\theta_{\pm}) = \sqrt{\frac{1 \pm R}{3}} \quad \text{with} \quad R = \frac{\omega - \omega_{\mathrm{N}}}{3\omega_{\mathrm{q}}} \ .$$

The absorption function line-shape as a function of frequency for an even distribution of the solid angle (random orientation of the molecules) can be split into

$$\chi''(\omega) \ \sim \ \sum_{\epsilon=\pm} \left| \frac{\mathrm{d}I_\epsilon(\theta)}{\mathrm{d}\omega} \right| = \sum_{\epsilon=\pm} \left| \frac{\mathrm{d}I_\epsilon(\theta)}{\mathrm{d}(\cos\theta_\epsilon)} \frac{\mathrm{d}(\cos\theta_\epsilon)}{\mathrm{d}\omega} \right|$$

$$\propto \ \sum_{\epsilon=\pm} \left| \frac{\mathrm{d}I_\epsilon(\theta)}{\mathrm{d}(\cos\theta_\epsilon)} \frac{1}{\omega_{\mathrm{q}}\sqrt{1 + \epsilon R}} \right| \ .$$

The signal will consist of two overlapping transitions, where the plus transition has a pole at $R = -1$ and $-1 \leq R \leq 2$ and the minus transition has a pole at $R = 1$ and $-2 \leq R \leq 1$.

The density of states, $\frac{\mathrm{d}(\cos\theta_\epsilon)}{\mathrm{d}\omega}$, can be convoluted with a Lorentzian function of width $A$ in order to include the broadening of the resonance lines due to spin-spin interactions with the surrounding dipoles and other effects, giving the shape function

$$F_\epsilon(R, A) = \int_{-\epsilon}^{2\epsilon} \frac{\epsilon\,\mathrm{d}x}{\sqrt{1 + \epsilon x}} \frac{A/\pi}{A^2 + \epsilon^2(x - R)^2}$$

$$= \frac{2A}{\pi} \int_0^{\sqrt{3}} \frac{\mathrm{d}y}{y^4 - 2(1 + \epsilon R)y^2 + A^2 + (1 + \epsilon R)^2}$$

where $y = \sqrt{1 + \epsilon x}$ was substituted. The solution to the convolution integral above is analytic [28], leading to the function [29]

$$F_\epsilon(\omega) = \frac{1}{2\pi\varrho} \times$$

$$\left\{ 2\cos(\alpha/2) \left[ \arctan\left( \frac{Y^2 - \varrho^2}{2Y\varrho\sin(\alpha/2)} \right) + \frac{\pi}{2} \right] \right.$$

14

$$+ \sin(\alpha/2) \ln\left(\frac{Y^2 + \varrho^2 + 2Y\varrho\cos(\alpha/2)}{Y^2 + \varrho^2 - 2Y\varrho\cos(\alpha/2)}\right)\right\} \tag{7}$$

where $\varrho^2 = \sqrt{A^2 + (1+\epsilon R)^2}$ and $\cos(\alpha) = (1+\epsilon R)/\varrho^2$ and $Y = \sqrt{3}$ was the upper integration limit.

The frequency dependence of the intensity factors, $\frac{dI_\pm}{d(\cos\theta_\pm)}$, is a very important contribution to the line-shape of broad signals such as those of nitrogen. Including the quadrupole coupling terms in the filling of the energy states, their differential populations are

$$dn_1 = \mathcal{N}^{-1} e^{\beta\hbar\omega_N + \beta\hbar\omega_q\lambda(\theta)} d(\cos\theta)$$
$$dn_{-1} = \mathcal{N}^{-1} e^{-\beta\hbar\omega_N + \beta\hbar\omega_q\lambda(\theta)} d(\cos\theta)$$
$$dn_0 = \mathcal{N}^{-1} e^{-2\beta\hbar\omega_q\lambda(\theta)} d(\cos\theta)$$

where $\lambda(\theta) = [3\cos^2(\theta) - 1]$, $\mathcal{N} = \sum_m e^{-\beta E_m}$ is the normalization, and $\beta = (kT_s)^{-1}$ with $T_s$ being the spin temperature of the system. Using $r = e^{\beta\hbar\omega_N}$ which is the same quantity as in Eq. (4), the intensity factor for the plus transition is [29]

$$\frac{dI_+}{d(\cos\theta_+)} = \frac{dn_1 - dn_0}{d(\cos\theta_+)} = \frac{r^{1+\vartheta\lambda} - r^{-2\vartheta\lambda}}{r^{1+\vartheta\lambda} + r^{-2\vartheta\lambda} + r^{-1+\vartheta\lambda}}$$
$$\overset{\lambda=R}{\Longrightarrow} \frac{r^2 - r^{1-3\vartheta R}}{r^2 + r^{1-3\vartheta R} + 1} \tag{8}$$

and the intensity factor for the minus transition is

$$\frac{dI_-}{d(\cos\theta_-)} = \frac{dn_0 - dn_{-1}}{d(\cos\theta_-)} = \frac{r^{-2\vartheta\lambda} - r^{-1+\vartheta\lambda}}{r^{1+\vartheta\lambda} + r^{-2\vartheta\lambda} + r^{-1+\vartheta\lambda}}$$
$$\overset{\lambda=-R}{\Longrightarrow} \frac{r^{1+3\vartheta R} - 1}{r^2 + r^{1+3\vartheta R} - 1} \tag{9}$$

where the ratio $\vartheta = \omega_q/\omega_N$ is the relative strength of the quadrupolar and dipolar interactions. The relation $[3\cos^2(\theta) - 1] = \epsilon R$ was used in the last two equations to write the frequency dependence of the transition factors explicitly.

Putting all of the pieces together, the absorption function now becomes

$$\chi''(\omega) \propto \frac{1}{\omega_q}\left\{\left[\frac{r^2 - r^{1-3\vartheta R}}{r^2 + r^{1-3\vartheta R} + 1}\right] F_+(R, A)\right.$$
$$\left. + \left[\frac{r^{1+3\vartheta R} - 1}{r^2 + r^{1+3\vartheta R} + 1}\right] F_-(R, A)\right\} . \tag{10}$$

Fig. 7 illustrates how parts of Eq. (10) combine to make a nitrogen signal of 10 % polarization. Contrary to the deuteron signal in butanol [29], the plus transition corresponds to the left peak while the minus transition corresponds to the right peak. Due to the intensity factors, the signals have a much higher gain toward the right side, or toward higher frequencies for such broad signals. Another important fact is that the intensity factor ratio is not constant across the total signal width. If one would set $\vartheta = 0$ in Eqs. (8) and (9), then the ratio of the intensity factors would be $dI_+/dI_- = r$, the asymmetry parameter. Thus, while this ratio is a good parameter that is closely related to the polarization of thin quadrupole broadened signals like those of deuterons, it is not related in an evident way to the polarization of wide signals such as those of nitrogen. The proper way to obtain $r$ is by fitting Eq. (10) to the data.

In Fig. 8, a demonstration of the features of the line-shape of Eq. (10) is made. In the left-hand plot, a comparison of the line-shapes for positive and negative signals is shown. Note that for both ±10 % polarization, the right peak is taller than the left one. This is caused by the strong frequency dependence of the intensity factors. In the right-hand plot, the peak height ratio

$$\rho = \frac{dI_-(R=1)}{dI_+(R=-1)} \tag{11}$$

for a large range of nitrogen polarizations is predicted at 2.5 T. The $\rho$ ratio is useful because it can be estimated directly from the measured signals, whereas $r$ can not. This shows that
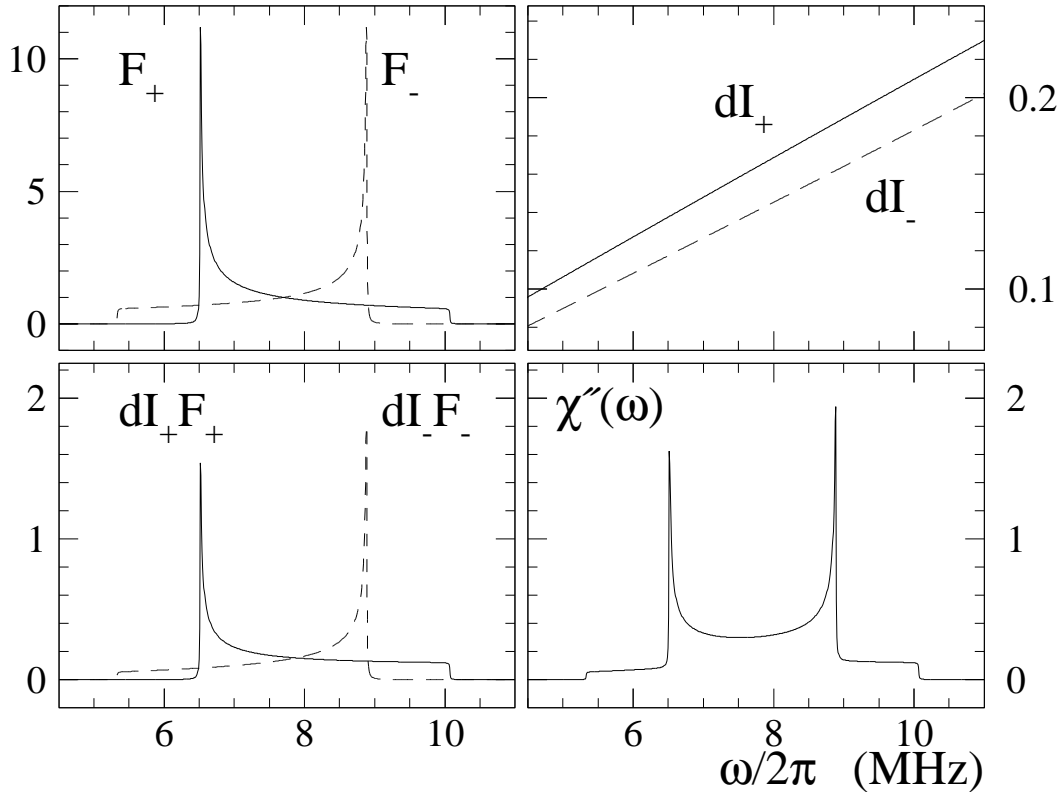
15

Figure 7: An example of how a nitrogen absorption function is composed of its parts. *Top Left*: The two $F_\pm$ shape functions. *Top Right*: The $\mathrm{d}I_\pm/\mathrm{d}(\cos\theta_\pm)$ intensity factors. *Bottom Left*: The products $[\mathrm{d}I_\pm/\mathrm{d}(\cos\theta_\pm)]F_\pm$. *Bottom Right*: The absorption function $\chi'' = \sum_\pm[\mathrm{d}I_\pm/\mathrm{d}(\cos\theta_\pm)]F_\pm$. The vertical scales are arbitrary, but consistent.

even at zero polarization, the ratio converges to $\rho = 1.39$, not $\rho = 1$, which is due to the intensity factors. As the polarization grows, the peak height ratio for positive polarizations decreases, crossing unity at about 28 % polarization whereas the peak height ratio for negative polarizations increases as the polarization magnitude grows. If the quadrupole splitting were negligible, the peak height ratio would be unity at zero polarization because the intensity factors would have no frequency dependence. As the quadrupolar splitting increases, the frequency dependence of the intensity factors becomes more pronounced and the peak height ratio is unity towards more positive polarizations.

## 5.2 Proton-Nitrogen Cross-Calibration

At 1 K and 2.5 T, TE polarization of nitrogen is about 40 % as large as the deuteron's. Furthermore, the absorption function is spread out over 4.8 MHz as opposed to the 260 kHz line width of the deuteron. Considering also that the density of nitrogen nuclei in ammonia is lower than the deuteron density in the standard alcohol materials, then the TE signal coming from nitrogen at 1 K is about two orders of magnitude smaller than that of deuterons. The noise of the NMR system is already at the edge of what is required for making a deuteron TE calibration. Thus, a direct TE calibration for nitrogen was impossible.

The only unknown factors in the relationship between the NMR signal area and the polarization are the gain of the Q-meter and the filling factor of the material in the coil. Once an NMR system is calibrated, it can be used to measure the polarization of any spin species as long as differences in the magnetic moments and the number of nuclei are taken into account.
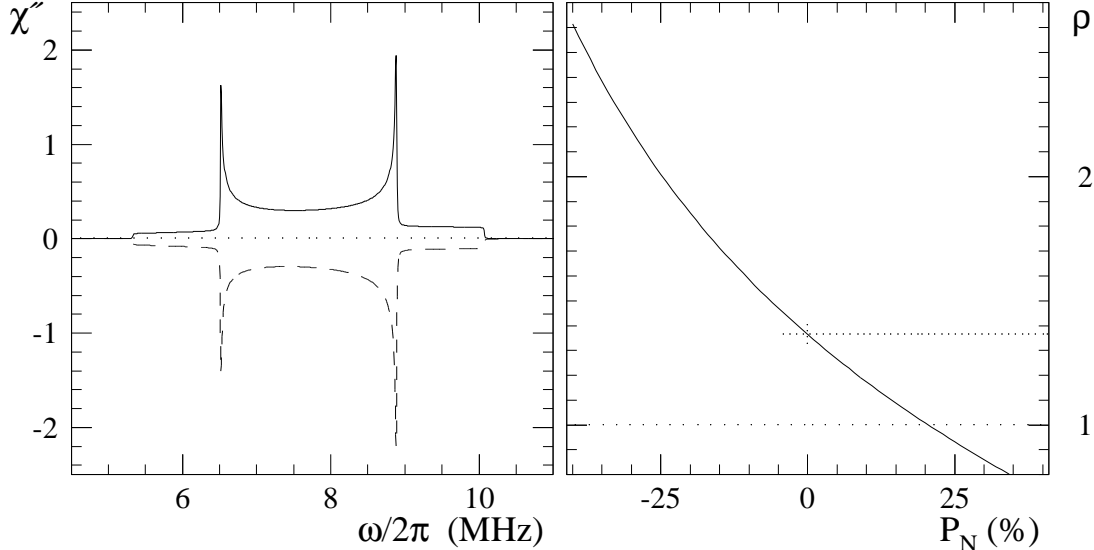
Figure 8: A study of the line-shapes for positive and negative polarizations. *Left*: Comparison of positive (solid) and negative (dashed) line-shapes for polarizations of $\pm 10\%$ ($r$=1.16 or 0.86). *Right*: Prediction of the peak height ratio, $\rho$, versus the nitrogen polarization from our line-shape using $\omega_{\mathrm{q}}/2\pi = 0.395\,\mathrm{MHz}$ and $\omega_{\mathrm{N}}/2\pi = 7.7\,\mathrm{MHz}$. A detailed explanation of the plots is in the text. Eqs. (10) and (11) were used to calculate these functions.

Therefore, the protons in the ammonia were used to calibrate the nitrogen NMR system.

The starting point for the cross-calibration is to consider a ratio of nitrogen to proton polarizations, written

$$\frac{P_{\mathrm{N}}}{P_{\mathrm{p}}} = \frac{g_{\mathrm{p}}^2 I_{\mathrm{N}} N_{\mathrm{p}} \mathcal{A}_{\mathrm{N}}}{g_{\mathrm{N}}^2 I_{\mathrm{p}} N_{\mathrm{N}} \mathcal{A}_{\mathrm{p}}}$$

where $\mathcal{A} = \int_0^\infty \chi''(\omega)\mathrm{d}\omega$ using Eq. (2) for the polarization. The $g$-factors are $g_{\mathrm{p}} = 2.793$ and $g_{\mathrm{N}} = 0.4038$ and $N_{\mathrm{p}} = 3N_{\mathrm{N}}$. Therefore, the nitrogen polarization is

$$P_{\mathrm{N}} = 287 \times \mathcal{A}_{\mathrm{N}} \times \frac{P_{\mathrm{p}}}{\mathcal{A}_{\mathrm{p}}} = 287 \times \mathcal{A}_{\mathrm{N}} \times \mathcal{K}_{\mathrm{p}} \tag{12}$$

where $\mathcal{K}_{\mathrm{p}} = P_{\mathrm{p}}/\mathcal{A}_{\mathrm{p}}$ is simply the calibration constant for protons.

The N/p-coil was calibrated at 1 K with proton signals by moving the magnetic field to a value where the proton Larmor frequency corresponds to the Larmor frequency at which the nitrogen signals were measured. This ensured that the Q-meter gain did not change. Once the cross-calibration constants were determined for the nitrogen coil, the polarization of the nitrogen was obtained using Eq. (12) and the area of the reconstructed signals, like the one shown in Fig. 9. The calibration constants were determined with a 2.5% relative error.

### 5.3   Measurement of the Nitrogen Absorption Function

In a 2.5 T field, the Larmor frequency of the nitrogen nuclei is $\omega_{\mathrm{N}}/2\pi = 7.7\,\mathrm{MHz}$ and their quadrupolar coupling constant is about $\omega_{\mathrm{q}}/2\pi = 0.4\,\mathrm{MHz}$ in solid ammonia at low temperatures [22]. Thus, the two peaks of the absorption function occurring at $\omega_{\mathrm{N}}/2\pi \pm 3\omega_{\mathrm{q}}/2\pi$ should be found around 6.5 MHz and 8.9 MHz. The sweep width required to pick up both peaks is about 2.4 MHz while in order to pick up the whole signal, including the shoulders, at least a 4.8 MHz sweep would be required. The ability of the Q-meter to detect an absorptive signal requires that this signal width be a small fraction of the Larmor frequency. Since it was beyond the possibilities of the Q-meters to measure the whole nitrogen signal with one sweep, only two small pieces of the nitrogen absorption function were measured by moving the magnetic field.

17

The sweeping frequency could not be changed since both pieces of the signal needed to be taken in precisely the same way and because the Q-meter tuning depends on the frequency range. In ammonia, the dipolar broadening is very small and each peak of the nitrogen signal is able to be measured with about a 100 kHz sweep width. However, a minimum of 200 kHz is needed to encompass an entire proton signal, which was needed to calibrate the system as described in §5.2.

A Larmor frequency of 6.47 MHz was chosen such that the corresponding field was 2.1 T and the Q-meter was swept over 200 kHz. The positions of the peaks were found at 1.68 T and 2.45 T, which are not symmetric about 2.1 T. This can be explained by including second order terms [20] in the calculation of the energy levels of Eq. (6), which shift the position of both peaks by the same amount towards higher Larmor frequencies (lower fields). The exact energy levels for this system were calculated which showed that the second order calculation was sufficient.

The quadrupole coupling parameter $\omega_q$ can be calculated from the field values where the peaks occurred when using a frequency of 6.47 MHz. The calculation is

$$6\omega_q/2\pi = (2.45 \text{ T} - 1.68 \text{ T})\frac{6.47 \text{ MHz}}{2.1 \text{ T}} = 2.372 \text{ MHz},$$

yielding a value of $\omega_q/2\pi = 0.395$ MHz. This agrees with the value of $\omega_q/2\pi = 0.396$ MHz, measured at 77 K and extrapolated down to zero temperature [22]. With this information, the algorithm for measuring the nitrogen absorption function consisted of the following steps:

 – A Larmor frequency of 6.47 MHz was chosen.
 – The Q-curve for the left (plus) peak of the signal was measured at 2.6 T.
 – The plus peak was measured at 2.45 T.
 – The Q-curve for the right (minus) peak of the signal was measured at 1.6 T.
 – The minus peak was measured at 1.68 T.

At first, a 200 kHz sweep was used but it was changed to 300 kHz because a larger sweep width was better for determining the area of the proton signals used in the cross-calibration. The calibration was done for both sweep widths. The Q-curves were taken in the pedestal area where the absorption function does not vary strongly over the scan width. This measures the shape of the Q-curve well enough, but the absolute magnitude is wrong by an additive constant. Since the pedestal is much smaller than the residual background caused by the drifting of the NMR system, this constant can be accounted for when the nitrogen signal pieces are put together and fit to the theoretical shape of the absorption function.


## 5.4 Reconstruction of the Nitrogen Absorption Function

The fitting algorithm must take into account that only two pieces, amounting to roughly 12 % of the 4.8 MHz signal width, can be measured from the nitrogen signal and that these pieces have different residual backgrounds since they are measured serially in time with the same Q-meter. Typically, the residual background is well described by a third order polynomial. Thus, the model used to fit the nitrogen signals which compensates for the two different backgrounds was

$$S(\omega) = \begin{cases} \mathcal{C}\chi''(\omega, \vartheta_{2.5}) + \sum_i a_i\,\omega^i & \text{for} \quad R < 0 \\ \mathcal{C}\chi''(\omega, \vartheta_{1.7}) + \sum_i b_i\,\omega^i & \text{for} \quad R > 0 \end{cases} \tag{13}$$

where $i = 0, \ldots, 3$ and the constant $\mathcal{C}$ and the absorption function given in Eq. (10) are the same for both pieces except that a different value of $\vartheta$, corresponding to the fields at which the signals were taken, can be used for each peak. The justification for using two values of $\vartheta$ will be given in the following section. The fit parameters are $\mathcal{C}$, $r$, $A$, $\omega_N$, $\omega_q$, the $a_i$, and the $b_i$ amounting to 13 in total.
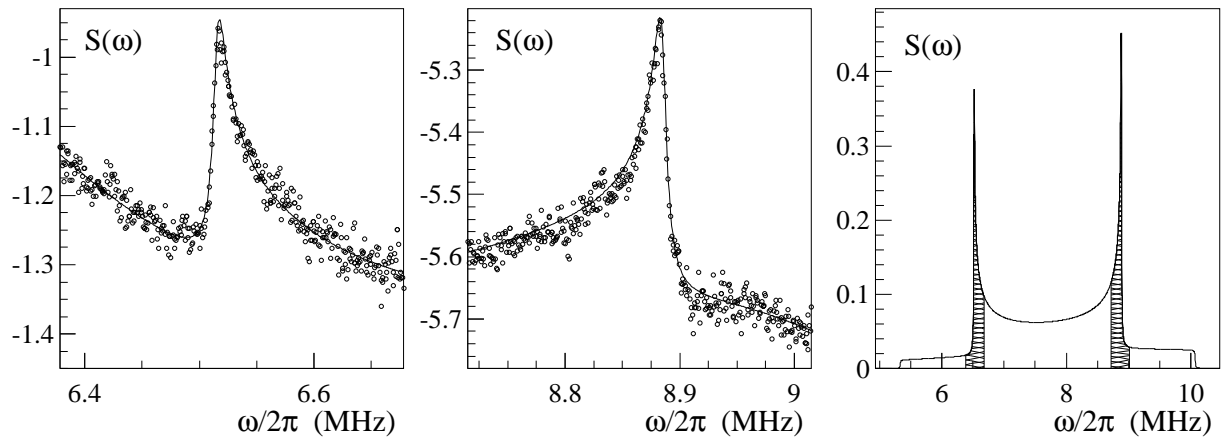
18

Figure 9: The two measured parts of a nitrogen subtracted signal and the entire signal reconstructed from the line-shape model. *Left and Middle*: The measured left and right signal peaks (plus and minus transitions). The solid lines are fits to the dots which are the raw data points. *Right*: The reconstructed signal with the residual background removed. The hashed areas represent the measured regions. The polarization of this signal is determined to be $P_N = 9\%$ from both the area and asymmetry methods.

Fig. 9 shows the two measured pieces of a nitrogen subtracted signal with the fit of the function in Eq. (13) superimposed. The scale of the raw data is radically different due to the drifting of the NMR system between the times when the Q-curves and signals were taken for each section of the nitrogen signal. The structure of the absorption function around the peaks is a very dominating feature and, for this reason, the absorption function can be distinguished from the background even though the Q-curve was actually taken on the pedestal of the signal and not completely outside.

The polarization can be directly calculated from the fit parameter $r$ via the Eq. (4) and is known as the "asymmetry method". In addition to $r$, the fit determines the other parameters of the NMR signal such as $A$, $\omega_q$, $\omega_N$ and $\mathcal{C}$. Once these values were known, the full signal could be calculated over all values of frequency. For example, the whole signal shown in Fig. 9 was reconstructed in this way. From the area of the reconstructed signal, the polarization could be determined by multiplying the area by the cross-calibration constant.

## 5.5 The Nitrogen Signal Peak Height Ratio

The evolution of the peak height ratio as a function of its polarization was predicted in §5.1. Once the polarization of the nitrogen signals was determined by the procedure above, and the peak height ratio was estimated from the raw signals, a test of the prediction was made.

There are two possible ratios which can be compared to the data. One ratio assumes that the populations of the non-equidistant nitrogen states, which were created while polarizing the protons at 2.5 T, are frozen in and remain constant while the field is ramped to measure the signals. This is the ratio plotted in Fig. 8. This would imply that the intensity factors are the same at both field values where the peaks are measured, and that only one value of $\vartheta$, corresponding to 2.5 T, should be used. Approximately 25 minutes elapsed between the measurement of the two parts of the nitrogen signals. Therefore, another possibility is that the populations of the states relax when the field is lowered such that a single spin temperature can always be ascribed to the system, and values of $\vartheta$ corresponding to the field at which the signals are measured should be used. Furthermore, we approximate that the spin temperature
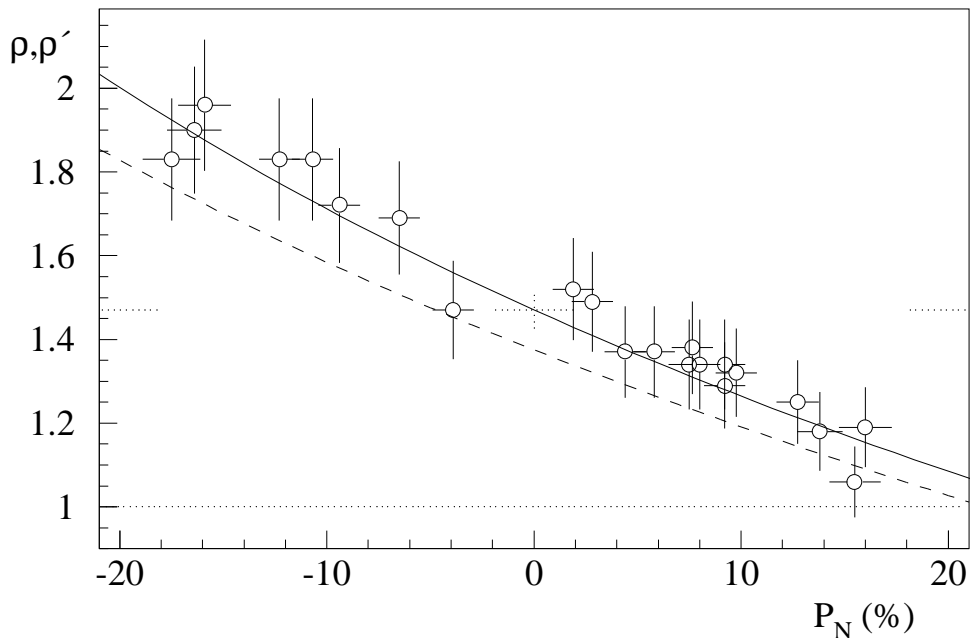
Figure 10: A comparison of the predicted peak height ratio to the experimentally measured ratio. The data points are the results obtained by estimating the peak heights from the raw signals. The solid line is the prediction if separate values of $\vartheta$ are used for each peak ($\rho'$), whereas the dashed line corresponds to the ratio when only the 2.5 T value of $\vartheta$ is used ($\rho$). The measured value $\omega_{\mathrm{q}}/2\pi = 0.395\,\mathrm{MHz}$ was used.

of the nitrogen changes proportionally to the Larmor frequency, so that the factor $r = e^{\beta\hbar\omega_{\mathrm{N}}}$ remains constant. These two ideas are summed up by the two equations

$$\rho = \frac{\mathrm{d}I_-(R=1, \vartheta=0.051)}{\mathrm{d}I_+(R=-1, \vartheta=0.051)}$$

and

$$\rho' = \frac{\mathrm{d}I_-(R=1, \vartheta=0.075)}{\mathrm{d}I_+(R=-1, \vartheta=0.052)} \ .$$

with $\vartheta = 0.051$, $\vartheta = 0.052$ and $\vartheta = 0.075$ corresponding to 2.5 T, 2.45 T and 1.68 T fields, respectively. As can be seen in Fig. 10, the evolution calculated using a 2.5 T field does not agree well with the data. However, a better agreement is observed if the ratio is calculated using a different field value for each transition. Therefore, we conclude that the populations vary with the field and the system remains approximately in thermal equilibrium.

## 5.6   Corrections to Nitrogen Polarization

As mentioned in the introduction, the large quadrupole splitting of the nitrogen system necessitates a more careful calculation of the nitrogen polarization in terms of the spin temperature. The polarization can be calculated from its definition

$$\begin{aligned} P \ &= \ \frac{\langle I_z \rangle}{I} = \frac{\mathrm{Tr}\{\rho I_z\}}{I} \\ &= \ \frac{\mathrm{Tr}\{e^{-\beta\mathcal{H}} I_z\}}{I\,\mathrm{Tr}\{e^{-\beta\mathcal{H}}\}} = \frac{\sum_m e^{-\beta E_m} \langle m | \, I_z \, | m \rangle}{I \sum_n e^{-\beta E_n}} \end{aligned} \tag{14}$$

where $\mathcal{H}$ is the Hamiltonian of the system [20]. Taking the energy levels calculated to first order in perturbation theory from Eq. (6), and the zeroth order states, yields the $\theta$-dependent

20

polarization relation

$$P_{\mathrm{N}}(\theta) = \frac{r^2 - 1}{r^2 + 1 + r\mathcal{R}}$$

$$\equiv \frac{\tanh(\beta\hbar\omega_{\mathrm{N}}/2)}{(2 + \mathcal{R}) + (2 - \mathcal{R})\tanh^2(\beta\hbar\omega_{\mathrm{N}}/2)}$$

where $\mathcal{R} = e^{-3\beta\hbar\omega_{\mathrm{q}}(3\cos^2(\theta)-1)}$. Averaging over the solid angle leads to

$$P_{\mathrm{N}} = \int_0^1 P_{\mathrm{N}}(\theta)\mathrm{d}(\cos\theta)$$

$$\approx \frac{r^2 - 1}{r^2 + r + 1}\left\{1 - \frac{6}{5}\frac{\vartheta^2 r \ln^2(r)}{r^2 + r + 1}\right\} \tag{15}$$

which becomes Eq. (4) as $\vartheta$ vanishes. The correction is in the range of fractions of a percent for nitrogen polarizations of 20 % and less for lower polarizations. Thus, Eq. (5) relating the nitrogen polarization to the proton polarization, assuming EST, is a good approximation. In addition, the polarization can be calculated with Eq. (4), once the parameter $r$ is known from fitting.

A small effect comes from the fact that $\langle I_z \rangle$ is smaller at lower fields because the matrix elements $\langle m|\,I_z\,|m\rangle$ in Eq. (14) become smaller due to the quadrupolar interaction. Since the electric field gradient axis is randomly distributed, the projection of the spin on the solenoid field, $I_z$, decreases. In our case the field was lowered from the nominal value of 2.5 T to 2.45 T and 1.68 T in order to measure the two parts of the N-14 absorption line. Thus the polarization at 1.68 T was underestimated. This effect was quantified by solving exactly for the eigenvalues and eigenstates of the Hamiltonian including quadrupolar interactions. Once the eigenstates were known, the matrix elements $\langle m|\,I_z\,|m\rangle$ were calculable. This effect depends on $\theta$ and vanishes at $\theta = 0$, i.e., at the shoulders. The average difference between $\langle I_z \rangle$ values calculated at 1.68 T compared to 2.45 T amounts to less than 1 % relative underestimate of the polarization.

Another small effect comes from the fact that also the NMR signal is smaller at lower field values due to the quadrupolar interaction. Through the use of Fermi's Golden Rule, one can write out the integral of the NMR signal as [18]

$$\int_{-\infty}^{\infty} \langle I_y \rangle \mathrm{d}\omega \propto \sum_{m=0,1} |\langle m|\,I_x\,|m - 1\rangle|^2$$

$$\times \left[\frac{e^{-\beta E_m} - e^{-\beta E_{m-1}}}{\sum_n e^{-\beta E_n}}\right]. \tag{16}$$

For the case of pure Zeeman splitting, Eqs. (14) and (16) reduce to the standard relation $\langle I_z \rangle \propto \int \langle I_y \rangle \mathrm{d}\omega$. However, when quadrupolar interactions are present, this relation is not generally valid. Using the solution for the exact states, calculation of this equation shows that the NMR signal is reduced at lower field values. The way to relate the NMR signal to the polarization is to calculate numerically the inverse spin temperature from Eq. (16), whose value is known from the integral of the calibrated NMR signal, and use that temperature in Eq. (14) to calculate the polarization. The result is that an NMR signal taken at 1.68 T is smaller by 4 % relative compared to an NMR signal taken at 2.45 T. Thus, integrating the NMR signals and multiplying by the cross-calibration constant, which was determined from a pure Zeeman system, will underestimate the polarization by about 2 % relative. This will be included in the systematic error.

## 6 Relating Proton and Nitrogen Polarization

In this section, the proton and nitrogen polarization measurements are used to make a test of the EST hypothesis. Cross relaxation between the proton and nitrogen spin systems is discussed. The effect of the nitrogen polarization on the measured scattering asymmetry is
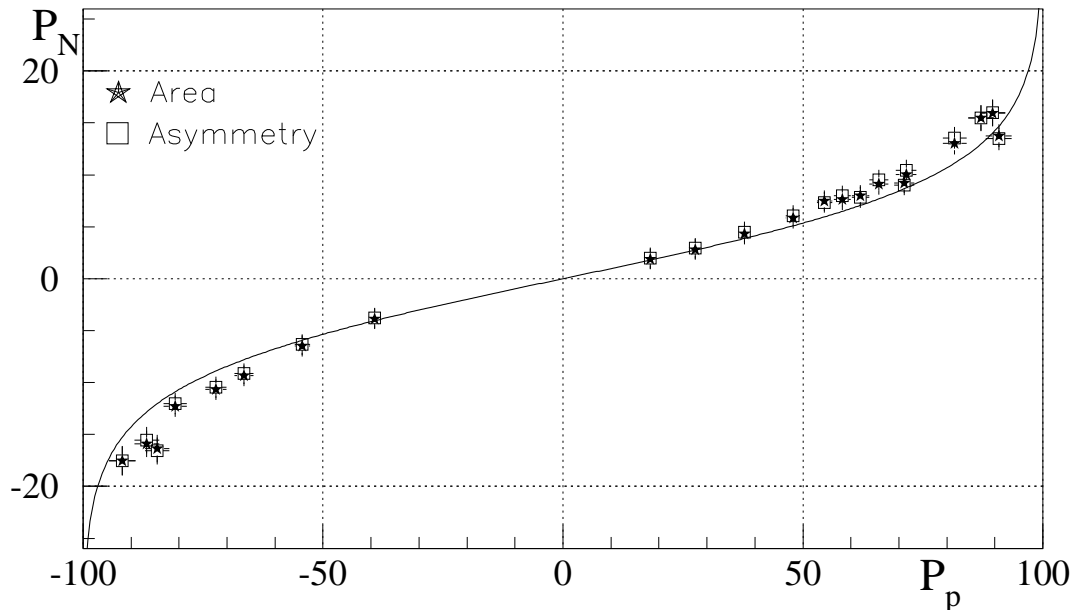
Figure 11: A test of the EST hypothesis in ammonia. The nitrogen polarization as determined by the cross-calibrated area and asymmetry methods is plotted as a function of the proton polarization. The EST curve (solid) was calculated from Eq. (15).

estimated.

## 6.1 A Test of the EST Hypothesis

A test of the EST hypothesis for ammonia was made for both positive and negative polarizations. The protons were polarized with DNP starting from zero and continuing to the highest possible value, stopping along the way to measure the nitrogen signals. The plot of the data in Fig. 11 supports an overall agreement with the EST prediction over a large range of polarizations.

The small but systematic deviation from exact EST behavior towards higher nitrogen polarization could be understood as a contribution from the differential solid state effect (DSSE). However, the DSSE fails to explain the microwave frequency dependence of the proton polarization [31] as the only DNP mechanism in ammonia. The deviations from EST in $^{15}NH_3$ [9, 10] are in the same direction as ours and of the same order of magnitude.

With the NMR signal area calculation relying largely on the line-shape model, a careful error analysis was required. The dominant error pertained to the residual background. For each nitrogen polarization measurement, several (up to 5) successive signals were taken for the plus peak before the field was lowered to take several signals for the minus peak. Analyzing all of the combinations yielded a relative statistical error of $\delta P_N/P_N = 2\%$ due to noise and different background drift amongst the signals. A further check was made using simulated signals. Left–right pairs of nitrogen signals were created for polarizations corresponding to our data using the line-shape model. Then, gaussian noise and third order polynomial residual backgrounds were added to them. The simulated signals were analyzed in the standard way and the polarization of the simulated and analyzed signals were compared. The residual background was more influential at low polarizations. The final error, including the considerations of §5.6 combined with the statistical uncertainty and error of the TE calibration, was estimated to be $|\delta P_N/P_N| \leq 8\%$ at polarizations exceeding 12% and $|\delta P_N| \leq 1\%$ below that due to the residual background.
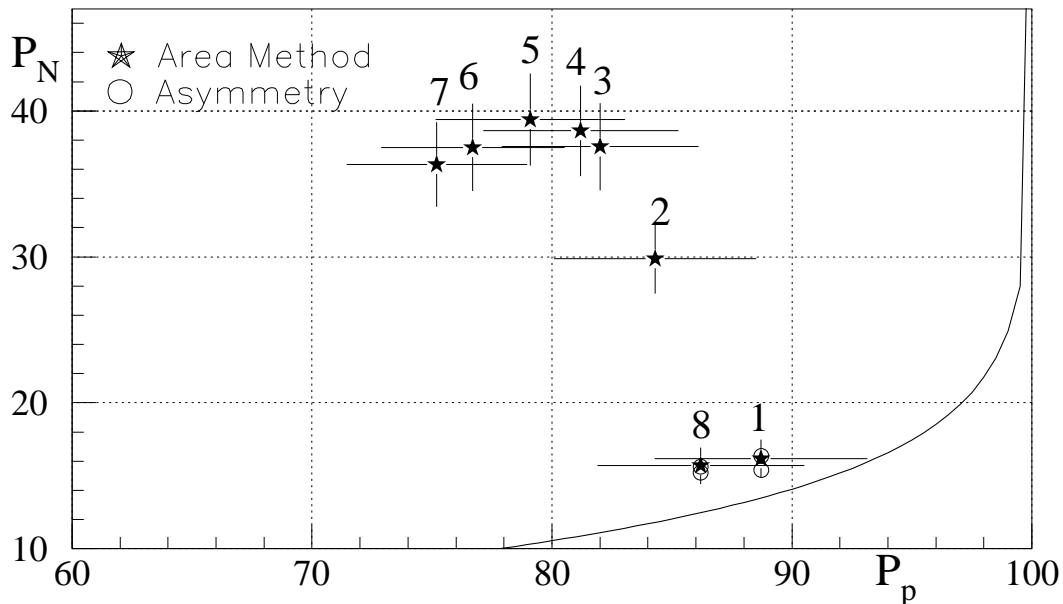
22

Figure 12: A plot of the cross relaxation properties of protons and nitrogen nuclei in ammonia. The numbers above the data points correspond to the chronological order in which the polarizations were measured. DNP was started between the points labeled 7 and 8. The EST curve (solid) is plotted for reference. The nitrogen polarization was determined by the area method for all points (stars). In addition, the asymmetry method (circles) was used for the first and last points (see text for details).

## 6.2  Cross Relaxation in the Ammonia System

In high magnetic fields the proton and nitrogen spin systems can be considered to be isolated from each other in the absence of microwaves because their Larmor resonance lines are very far apart. However, at low (near-zero) field values, the nitrogen nuclei will still have a quadrupolar splitting of $E_m = -2\hbar\omega_{\text{q}}(3m^2 - 2)$ and therefore a resonance at $6\omega_{\text{q}}/2\pi = 2.4\,\text{MHz}$ due to this. This corresponds to a proton Larmor frequency at $56\,\text{mT}$. Cross relaxation can then take place between the proton Zeeman and the nitrogen quadrupolar systems.

An investigation of this effect began with a high proton polarization of $89\,\%$ and nitrogen polarization of $16\,\%$. The magnetic field was reduced to $45\,\text{mT}$ and immediately raised back to $2.5\,\text{T}$ several times. After each of the resonance crossings, the proton and nitrogen signals were measured. Once the nitrogen polarization stopped increasing, DNP was started to see how fast the system would return to EST conditions. Fig. 12 shows the results of this exercise. After the first resonance crossing, the polarization of the nitrogen system increased dramatically. After the initial increase, the nitrogen polarization increased by smaller amounts and eventually begins to decay due to spin-lattice relaxation. A maximum nitrogen polarization of $40\,\%$ was reached and, after DNP, the system returned exponentially to the EST conditions with a relaxation time of about 25 minutes.

We found that the nitrogen system was not in thermal equilibrium after the cross relaxation (see below). This means that there was a separate spin temperature for each transition. Therefore, for fitting the nitrogen signals, a separate $r$ parameter was used in Eq. (10) for each transition. For all of the data points, the polarization values were determined by the area method. For the first and last points, two $r$'s were also used. Their fitted values produced consistent polarizations with the area method since they were taken under EST conditions, that is after DNP.

The non-equilibrium behavior is easy to understand by the fact that at low fields the $m = \pm 1$ states are nearly degenerate and lower in energy than the $m = 0$ state. In thermal equilibrium, the populations of the $m = \pm 1$ states would be nearly equal and different from the one of the $m = 0$ state. When the field is increased back to the Zeeman-dominated regime, the $m = 0, 1$ energy levels cross and spin flip-flop transitions would tend to rearrange the populations in such a way that at high field the spin system would obey the Boltzmann distribution. If the field sweep is too fast, the system does not stay in thermal equilibrium and one would expect to see enhanced tensor polarization $A \equiv \langle 3I_z^2 - I(I+1) \rangle / I^2$ at the end of the field sweep. This is exactly what was observed upon measuring the peak heights after the cross relaxation procedure. The peak height ratio had values near $\rho \approx 2$, instead of $\rho \lesssim 1$, for the nitrogen signals after the cross relaxation. The tensor polarization was about -7 % instead of the equilibrium value of 2 %. This is the justification for using independent $r$-parameters when fitting these non-equilibrium signals.

Cross relaxation could in principle be used to prepare a polarized nitrogen target. Let us estimate the maximum nitrogen polarization attainable in our conditions, neglecting the thermal relaxation. Assuming exact EST and a typical proton polarization of 90 %, the initial spin temperature of the two systems will both be 1.7 mK. Starting with the equation for the entropy $S = -k \sum_m n_m \ln(n_m)$ [32], the proton and "high-field" nitrogen entropies are

$$S_p = k \left[ \ln(R+1) - \frac{R \ln(R)}{R+1} \right]$$

and

$$S_N^H = k \left[ \ln(r^2 + r + 1) - \frac{(2r^2 + r)\ln(r)}{r^2 + r + 1} \right]$$

where $R = e^{\beta \hbar \omega_p}$ and $r = e^{\beta \hbar \omega_N}$ and the quadrupole splitting was neglected. If the spin systems are isentropically demagnetized by lowering the field from 2.5 T to 56 mT, the proton spin temperature reduces from 1.7 mK to 39 $\mu$K, directly proportional to the field change. However, instead of the previous equation for the high-field case, the entropy of the "low-field" nitrogen system considering only the quadrupolar interaction is described by

$$S_N^L = k \left[ \ln(1 + 2r^{6\vartheta}) - \frac{2r^{6\vartheta} \ln(r^{6\vartheta})}{1 + 2r^{6\vartheta}} \right]$$

where $\vartheta = \omega_q / \omega_N \approx 2.3$ at 56 mT. Solving this equation numerically and requiring that the entropy be the same as before yields a quadrupolar spin temperature of 230 $\mu$K for nitrogen, which is much higher than the proton spin temperature. This allows the proton system to cool the nitrogen system. Assuming perfect mixing, the final common spin temperature can be found from the energy balance. The heat transfer $Q = \int T \mathrm{d}S = \int T \left( \frac{\partial S}{\partial r} \right) \mathrm{d}r$ for the two cases is

$$Q_p = \hbar \omega_p \left[ \frac{1}{1 + R_f} - \frac{1}{1 + R_i} \right]$$

and

$$Q_N^L = 6\hbar \omega_q \left[ \frac{1}{1 + 2r_f^{6\vartheta}} - \frac{1}{1 + 2r_i^{6\vartheta}} \right]$$

where $R_i$ and $r_i$ are calculated at 39 $\mu$K and 230 $\mu$K, and $R_f$ and $r_f$ are calculated at the new equilibrium temperature. Numerically solving the heat transfer balance equation $3Q_p = -Q_N$ yielded 56 $\mu$K as a final temperature. Recalculating the entropy of the two systems shows that the total entropy increases by a factor 1.16.

Isentropical magnetization back to 2.5 T leads to spin temperatures of 2.5 mK and 420 $\mu$K for protons and nitrogen, corresponding to polarizations of 0.77 and 0.52, respectively. The fact that we did not reach this value is mostly due to spin-lattice relaxation. The field sweep is quite slow, 3 mT/s, and the relaxation is quick even for fields far above the final field of 56 mT at the 100 mK lattice temperature in which this experiment was done. With a lower lattice

temperature it should be possible to reach higher final nitrogen polarizations.

## 6.3 The Nitrogen Contribution to the Scattering Asymmetry

When a beam of polarized muons is scattered by an ammonia target, the measured asymmetry will come largely from the highly polarized protons with a small contribution from the slightly polarized nitrogen nuclei. The number of events reads

$$
\begin{aligned}
N^{\pm} &= n_{\mathrm{p}}\sigma_{\mathrm{p}}(1 \pm P_{\mathrm{b}}P_{\mathrm{p}}A_{\mathrm{p}}) \\
&+ n_{\mathrm{N}}\sigma_{\mathrm{N}}(1 \pm P_{\mathrm{b}}P_{\mathrm{N}}A_{\mathrm{N}}) + \sum_{A} n_{A}\sigma_{A}
\end{aligned}
$$

where $P_{\mathrm{b}}$ is the beam polarization, the $n$'s are the number of target nuclei, the $\sigma$'s are the unpolarized cross sections, and the $A$'s are the cross section asymmetries. The subscripts p, N, A refer respectively to proton, nitrogen, and all unpolarizable nuclei in the target such as those in the NMR coils and helium coolant. The superscript refers to parallel $(-)$ or anti-parallel $(+)$ longitudinal beam-target polarization configurations. The measured asymmetry is

$$
A_{\mathrm{m}} = \frac{N^{+} - N^{-}}{N^{+} + N^{-}} = fP_{\mathrm{b}}P_{\mathrm{p}}\left(A_{\mathrm{p}} + \frac{n_{\mathrm{N}}P_{\mathrm{N}}}{n_{\mathrm{p}}P_{\mathrm{p}}}\frac{\sigma_{\mathrm{N}}A_{\mathrm{N}}}{\sigma_{\mathrm{p}}}\right)
$$

where $f$ is the dilution factor of the protons in the target material. In the nuclear shell model, the spin-1 nitrogen nucleus is considered to be a spinless carbon core with an extra proton and neutron each in a $1p_{\frac{1}{2}}$ orbital state [33]. Assuming the nitrogen nucleus has $M_S = 1$, the proton and neutron must both have $M_J = \frac{1}{2}$ in order to account for the nitrogen spin. In the coupling scheme $J = L \otimes S \to \frac{1}{2} = 1 \otimes \frac{1}{2}$, the state of one of these two nucleons can be written as

$$
\left|\tfrac{1}{2}, \tfrac{1}{2}\right\rangle = \sqrt{\tfrac{2}{3}}\left|1, 1; \tfrac{1}{2}, -\tfrac{1}{2}\right\rangle - \sqrt{\tfrac{1}{3}}\left|1, 0; \tfrac{1}{2}, \tfrac{1}{2}\right\rangle
$$

where $|J, M_J\rangle$ is the total angular momentum state of the nucleon and $|L, M_L; S, M_S\rangle$ represents its composition from orbital and spin angular momentum. Thus, it is twice as likely that the proton and neutron will have their spins anti-aligned with the spin of the nitrogen nucleus. The nitrogen asymmetry reads

$$
\sigma_{\mathrm{N}}A_{\mathrm{N}} = -\tfrac{1}{3}\left(\sigma_{\mathrm{p}}A_{\mathrm{p}} + \sigma_{\mathrm{n}}A_{\mathrm{n}}\right) \approx -\tfrac{2}{3}\sigma_{\mathrm{d}}A_{\mathrm{d}} \tag{17}
$$

where $A_{\mathrm{n}}$ and $A_{\mathrm{d}}$ are the neutron and deuteron asymmetries and the d-state admixture of the deuteron is ignored. The same result is obtained if one considers the nitrogen nucleus to be a spinless core with a spin-1 particle orbiting in a $J = 1$ state. More detailed descriptions of the nitrogen nucleus, including the probability of the nucleons to be in higher orbital states [34] and modifications to the nuclear shell model [35] due to higher order corrections [36], lead to similar formulæ as Eq. (17) with different numerical factors. From the spread of these factors we estimate $\sigma_{\mathrm{N}}A_{\mathrm{N}} = -2 \times (0.33 \pm 0.08)\sigma_{\mathrm{d}}A_{\mathrm{d}}$. Thus, the measured asymmetry is now

$$
A_{\mathrm{m}} = fP_{\mathrm{b}}P_{\mathrm{p}}\left[A_{\mathrm{p}} - (0.034 \pm 0.009)A_{\mathrm{d}}\sigma_{\mathrm{d}}/\sigma_{\mathrm{p}}\right] ,
$$

where the values $P_{\mathrm{p}} = (89 \pm 2.5)\,\%$ and $P_{\mathrm{N}} = (13.5 \pm 1.1)\,\%$, corresponding to the average running conditions of SMC, were used. Using the measured values of the deuteron and proton cross sections, and the deuteron asymmetry, the correction factor ranges from $-2\,\%$ to $0.2\,\%$ depending on the kinematical region. The uncertainty in the contribution of the nitrogen nuclei to the measured asymmetry will be much smaller than the uncertainty caused by the error of the proton polarization measurement.

## 7    Conclusions

The polarization of nitrogen nuclei in ammonia was determined by both the asymmetry and area methods using the same theoretical spin-1 line-shape. A fitting paradigm was used to reconstruct the entire nitrogen NMR signal from the $12\,\%$ of the signal which was measured in two sections around the peaks. The sign of the electric field gradient in ammonia was deduced. A study of the effect of relaxation and DNP on the polarization of the nitrogen and proton

systems showed that the EST hypothesis is approximately valid during the DNP process up to the highest positive and negative polarizations of $\pm 90\%$.

A cross relaxation was observed when the magnetic field was swept to a low value. The nitrogen polarization was increased to 40 % while the proton polarization decreased to 74 %. The mechanism is understood as a cross relaxation at 56 mT where the proton Zeeman resonance crosses the nitrogen quadrupolar resonance. After starting DNP again, the system relaxed back to EST conditions in a time of about 25 minutes.

## Acknowledgements

## References

[1] B. Adeva et al., Phys. Lett. B **302** (1993) 533.

[2] B. Adeva et al., Phys. Lett. B **329** (1994) 399; Erratum, Phys. Lett. B **339**, (1994) 332.

[3] B. Adeva et al., Phys. Lett. B **357** (1995) 248.

[4] B. Adeva et al., Phys. Lett. B **336** (1994) 125.

[5] B. Adeva et al., submitted to Phys. Rev. D.

[6] J. Kyynäräinen, Nucl. Instr. Meth. A **356** (1995) 47.

[7] G. R. Court and W. G. Heyes, Nucl. Instr. Meth. A **243** (1986) 37.

[8] G. R. Court, W. G. Heyes, W. Meyer, and W. Thiel, in the proceedings of the *Fourth International Workshop on Polarized Target Materials and Techniques*, ed. W. Meyer (Bad Honnef, 1984) 53.

[9] D. G. Crabb and D. B. Day, Nucl. Instr. Meth. A **356** (1995) 9.

[10] B. van den Brandt, J. A. Konter, S. Mango, and M. Wessler, in the proceedings of the *9th Int. Symp. on High Energy Spin Phys.*, Vol. 2, (Springer-Verlag, New York, 1991) 307.

[11] A. Abragam and M. Goldman, Rep. Prog. Phys. **41** (1978) 395.

[12] K. Runkel, Diploma Thesis, Bonn-IB-94-30 (Bonn University, Germany, 1994) and references therein.

[13] The measurement technique is described in: S. Bültmann et al., Nucl. Instr. Meth. A **356** (1995) 102.

[14] S. Brown et al., in the proceedings of the *Fourth International Workshop on Polarized Target Materials and Techniques*, ed. W. Meyer, Bad Honnef (1984) 66.

[15] R. Dostert et al., ibid, 33.

[16] C. P. Slichter, *Principles of Magnetic Resonance*, (Springer-Verlag, New York, 1978), p. 49.

[17] M. Goldman, J. Mag. Res. **17** (1975) 393.

[18] M. Goldman, personal communication, February 1997.

[19] Y. K. Semertzidis, Nucl. Instr. Meth. A **356** (1995) 83.

[20] A. Abragam, *Principles of Nuclear Magnetism* (Clarendon Press, Oxford, 1961).

[21] M. H. Cohen and F. Reif, *Nuclear Quadrupole Effects in Solids*, in *Solid State Physics* **5** (Academic Press, New York, 1957).

[22] S. S. Lehrer and C. T. O'Konski, J. Chem. Phys. **43** (1965) 1941.

[23] E. A. C. Lucken, *Nuclear Quadrupole Coupling Constants* (Academic Press, London, 1969).

[24] G. R. Court et al., Nucl. Inst. Meth. A **324** (1993) 433.

[25] R. H. Dicke, Phys. Rev. **93** (1954) 99; Y. K. Kisselev et al., ZZh. Eksp. Teor. Foz. **94** (2) (1988) 344 [Sov. Phys. JETP **67** (1988) 413].

[26] N. F. Ramsey and E. M. Purcell, Phys. Rev. **85** (1952) 143.

[27] E. R. Andrew and R. Bersohn, J. Chem. Phys. **18** (1950) 159.

[28] I. S. Gradshteyn and I. M. Ryzhic, *Table of Integrals, Series, and Products* (Academic Press, New York, 1980).

[29] C. M. Dulya et al., accepted for publication in Nucl. Instr. Meth. A (1997).

[30] B. Adeva et al., Nucl. Instr. Meth. A **372** (1996) 339.

[31] H. Riechert, in the proceedings of the *5th High Energy Spin Symposium*, ed. G. Bunce, AIP Conf. Proc. 95 (1982) 520.

[32] F. Reif, *Fundamentals of Statistical and Thermal Physics* (McGraw-Hill, New York, 1965).

[33] J. M. Blatt and V. F. Weisskopf, *Theoretical Nuclear Physics* (Dover Publication Inc., New York, 1979).

[34] R. L. Huffman et al., Phys. Rev. C **35** (1987) 1.

[35] H. W. Baer et al., Phys. Rev. C **12** (1974) 921.

[36] B. A. Brown and B. H. Wildenthal, Phys. Rev. C **28** (1983) 2397.